

Applications of computation in acoustics: ultrasound bioeffects and underwater transmission loss uncertainty

by

Brandon Patterson

Dissertation proposal
submitted in partial fulfillment
of the requirements for the degree of
Doctor of Philosophy
Mechanical Engineering
University of Michigan
2016

Doctoral Committee:

Assistant Professor Eric Johnsen, Chair
Professor David R. Dowling
Professor William Schultz
Professor Douglas L. Miller
Professor J. Brian Fowlkes

TABLE OF CONTENTS

List of Acronyms and Abbreviations	iii
Abstract	iv
Chapter	
1 Introduction	2
I Ultrasound bioeffects	3
2 Introduction	4
2.1 Physical context	4
2.2 An overview of our work studying Ultrasound (US) bioeffects	5
3 <i>Past work:</i> Theoretical microbubble Dynamics at capillary breaching thresholds	6
3.1 Abstract	6
4 <i>Current work:</i> Diagnostic Ultrasound Induced Lung Hemorrhage	7
4.1 Introduction	7
4.2 Methods	11
4.3 Analysis	15
4.4 Preliminary results and discussion	19
4.5 Conclusions	22
4.6 Future Work	23
II Estimating transmission loss uncertainty in uncertain ocean environments.	30
5 <i>Past work:</i> Efficient estimation of the probability density function of transmission loss in uncertain ocean environments via area statistics	31
5.1 Abstract	31
Bibliography	32

LIST OF ABBREVIATIONS & ACRONYMS

CEUS Contrast-Enhanced Ultrasound

DG Discontinuous Galerkin

DUS Diagnostic Ultrasound

IC Inertial Cavitation

LH Lung hemorrhage

MC Monte Carlo

PD Pulse Duration

PDF Probability Distribution Function

PRF Pulse Repetition Frequency

RMI Richtmyer-Meshkov Instability

TL Transmission Loss

US Ultrasound

ABSTRACT

Numerical simulations are highly useful for approaching a wide range of problems within the field of acoustics. From submarine and whale sounds propagating across vast oceans to ultrasound striking microscopic bubbles in the blood stream behind layers of optically opaque tissue, there are a variety of contemporary acoustic problems with challenges that make them incredibly difficult or infeasible to investigate experimentally. Furthermore, many systems of acoustic interest such as the ocean and human body are immensely complex, rapidly changing, and poorly understood such that at any given time our best knowledge of the system is still fraught with uncertainty. Computation is used to overcome the difficulties of experimentation, explore a range of possibilities in uncertain systems, and to obtain detailed information about physical quantities that are not readily measurable. In this work, we present advancements in two very different areas of acoustics, made possible through the use of computation.

In the first part of this work, we investigate two problems related to biological effects of medical Ultrasound (US). The use of US for diagnostic and therapeutic purposes has grown very quickly over the last few decades, as technological advancements have allowed us to use US for everything from drug delivery and destruction of unwanted tissue to imaging of the internals of the human body. However, certain US procedures have been shown to cause unwanted biological effects that are still poorly understood because they occur on such small length and time scales that they cannot be directly observed as they occur in the body. We develop numerical models to investigate experimentally observed hemorrhage associated with Contrast-Enhanced Ultrasound (CEUS) and Diagnostic Ultrasound (DUS) of the lung. In doing so, we compare calculated cavitation bubble dynamics pertinent to CEUS to previously obtained experimental results to show that accepted thresholds for Inertial Cavitation (IC) are unlikely to be useful for predicting CEUS bioeffects. For the case of DUS of the lung, we propose a new physical damage mechanism based on ultrasonically-induced baroclinic torque at tissue air interfaces within the lungs. We perform analysis and simulations to demonstrate that, given certain simplifying assumptions, predictable deformation of the interface occurs via the proposed mechanism. We conclude that it is a feasible injury mechanism, which will be investigated in detail over the remainder of this thesis.

In the second part of this work we develop area statistics, a computationally efficient method for estimating the Probability Distribution Function (PDF) of acoustic Transmission Loss (TL) in uncertain ocean environments. This is useful in a variety of practical naval applications. The area statistics method is tested in four different ocean environments of varying geometry and acoustic properties with uncertain bathymetry, ocean floor properties, and sound speed profiles. We compare TL PDFs obtained with area statistics to those obtained via accepted, traditional Monte Carlo (MC) methods and find that the area statistics method is engineering-level accurate in 93% of tests in ocean environments with consistent bottom reflection, and can be produced with $\mathcal{O}(10^6)$ the computational effort required for the Monte-Carlo calculations.

Foreword

The proposed dissertation will present work using computation to make advancements in two separate, distinct areas of acoustics: ultrasound bioeffects and acoustic transmission loss uncertainty quantification in uncertain ocean environment. Hence this proposal will also be split into two parts along these lines. A summary of previous work in each area will be presented along with proposed future work in the area of ultrasound bioeffects that will be performed to complete the dissertation.

CHAPTER 1

Introduction

The purpose of this introduction is to set the stage for the proposed dissertation research. The problems we approach in this work are all problems of interest, current to the field of Acoustics. Broadly, acoustics is the study of sound. In practice, this study is not limited to just the kinds of sound that can be heard by humans, but rather any molecular scale vibrations traveling throughout a media. As sounds both natural and man-made are ubiquitous, it is a topic that has intrigued man for quite some time and attracted much attention and study. As such, we have gained not only an understand the physical nature of sound, but have also learned to harness it as a tool. Because sound waves travel reflect, transmit, and scatter in a mathematically describable way, they are ideally suited for gathering information in certain situations. Because they carry mechanical energy that can be focused, concentrated, and in some instances converted into other types of energy, such as heat, they can also be a powerful tool for physically altering an environment. In some applications of interest, attempts to use acoustics to gather information, can unintentionally lead to physical modification of the system, such is the case when DUS for medical imaging leads to unintended biological effects, or ultrasound bioeffects as we will refer to them from here on out.

Many problems of contemporary acoustic interest present challenges that make them difficult to investigate completely through direct experimentation. Some problems, such as certain ultrasound bioeffects, often involve physical processes that occur over such small length and time scales that they cannot be directly observed. When these phenomena are replicated in simplified lab experiments, as they frequently are, physical quantities of interest, like stress, are not always readily measurable. Other problems may call for experiments that are prohibitively costly and time-intensive, as is often the case in underwater and ocean acoustics experiments which can require long cruises with extensive personnel and equipment. Furthermore, in complex acoustic environments like the ocean or human body, we rarely have sufficient information to precisely and accurately describe the system of interest without a high degree of uncertainty. In instances such as these, where direct experimentation is infeasible or unable to provide the desired information, carefully designed numerical experiments can be useful for providing insight into the problem at hand.

The unifying theme of the work presented here is the use of computation to approach modern problems in acoustics. The two main areas of research considered are Ultrasound (US) bioeffects and underwater acoustic uncertainty. In the first part of this work, we investigate two problems related to biological effects of medical US. Specifically, we simulate physics associated with CEUS and DUS of the lung, which have both been shown to be capable of causing hemorrhage in mammals, in order to investigate the damage mechanism behind each. In the second part of this work we develop and test area statistics, a computationally efficient method for estimating the PDF of acoustic TL in uncertain ocean environments, which is useful in naval applications. As these areas are appreciably different, we will refer the reader to later portions of this document and to the authors relevant submitted and published works for more detailed introduction and background on each problem.

Part I

Ultrasound bioeffects

CHAPTER 2

Introduction

The purpose of this chapter is two fold. First, we aim to provide a general physical context for the work presented in this part of the thesis proposal. Second, we will provide a brief overview of the work to be presented and its significance. For a more detailed overview of the relevant literature, the reader is referred to later parts of this document, and to this authors published works.

2.1 Physical context

Diagnostic Ultrasound (US) has proven to be among the safest and most powerful medical imaging tools currently available. Its use has become ubiquitous throughout modern medicine. The basic physical principle underlying this technology is the scattering of sound at material interfaces. In practice, high-frequency, typically MHz range, acoustic waves and pulses are created at the surface of the body using a piezoelectric US transducer. These vibrations propagate via an acoustic coupling medium from the transducer into the tissue and scatter at changes in the material properties of the medium. More simply, some of the sound echoes whenever it moves from one tissue to another, or hits a cavity in the body. These echoes are then picked up by a receiver and recorded. This echo signal is processed to obtain real-time images of the scattering surface.

While clinical US is typically safe there are specific instances during which US can interact with tissue in such a way that the tissue is physically altered. These effects to the body are referred to as US bioeffects. Understanding these US-tissue interactions is important for the development of safe, effective US techniques (Dalecki, 2004). While the entire field of therapeutic US is focused on intentionally causing bioeffects in a way that is beneficial to the patient, diagnostic US is a different story. Bioeffects that occur during diagnostic US typically take the form of unintended hemorrhage, tissue damage, or cell death. Depending on the physical damage mechanism responsible, these bioeffects are broadly classified into two groups, thermal and non-thermal (O'Brien & Miller, 2007). The first group, thermal bioeffects are characterized by deposition of acoustic energy into tissue as heat. At the cellular and molecular scales, this can lead to the release of highly reactive free radicals, protein denaturation, and ultimately tissue damage and death. Little else will be said about thermal bioeffects, as the bioeffects problems of interest to this work are a result of non-thermal mechanisms.

The bulk of known non-thermal bioeffects are attributed to acoustically-induced cavitation. Acoustic cavitation is the phenomenon by which gas nano and microbubbles, called cavitation nuclei, are cyclically grown by low pressures within the US field and then collapsed high pressures within the field. Cavitation can be divided into two categories, stable cavitation, also called gas bubble activation, and Inertial Cavitation (IC), formerly referred to as transient cavitation. Stable cavitation typically occurs for low US intensity and is characterized by bubbles periodically oscillating around an equilibrium radius for multiple acoustic cycles. IC typically occurs for higher ultrasound intensities. During IC the bubble dynamics during collapse are dominated by the inertia of the surrounding fluid. The bubble collapses violently to a tiny fraction of its original size and then explosively rebounds back. There are variety of physical phenomena associated with IC that may be responsible for observed US bioeffects. Upon collapse, the pressure and temperature within the bubbles spike, often reaching billions of pascals and thousands of Kelvin respectively. Due to the pressure difference between the vapor/gas mixture within the bubble at collapse and the

surrounding media, the collapsed bubble can emit a powerful shock wave. When cavitation is triggered near a rigid surface, the bubble can collapse in a radially asymmetric fashion causing a high speed “re-entrant” jet of liquid to impinge upon the surface, effectively striking the surface with a liquid hammer. If cavitation occurs at an appropriate distance from a non-rigid surface, such as soft tissue boundaries and blood vessel walls, the jet can impinge away from the surface, potentially invaginating the surface (Brujan, 2011). One type of Diagnostic Ultrasound (DUS) for which cavitation is of particular concern is Contrast-Enhanced Ultrasound (CEUS), which uses contrast-agent microbubbles injected into patients bloodstream to act as additional scattering surfaces. These microbubbles can also serve as cavitation nuclei and have been associated with a variety of US bioeffects.

Another non-thermal US bioeffect of interest is DUS-induced Lung hemorrhage (LH), which is the only known bioeffect of non-contrast DUS known to occur in mammals. Despite the fact that this phenomenon was first observed in mice over twenty years ago (Child *et al.*, 1990), the underlying physical damage mechanisms remain unknown. Research has shown that thermal damage mechanisms are unlikely as DUS-induced lung lesions do not appear similar to those induced by heat (Zachary *et al.*, 2006). Furthermore, cavitation mechanisms do not appear to be responsible, as the severity of DUS-induced LH in mice increased under raised hydrostatic pressure (O’Brien *et al.*, 2000) and was unaffected by the introduction of US contrast agents into subjects. Both of these results are inconsistent with what is expected of IC-induced bioeffects. Works by Tjan & Phillips (2007, 2008) model the evolution of an inviscid, free surface subjected to a Gaussian velocity potential and find that this can lead to the ejection of liquid droplets. They go on to say that DUS of the lung may similarly lead to the ejected of droplets capable of puncturing the air-filled sacs within the lung. This problem is central to the our present and future work, and makes up the bulk of this proposal. As such, a far more in-depth literature review will be provided in Chapter 4.

2.2 An overview of our work studying US bioeffects

For the proposed dissertation, we will discuss our work studying two ultrasound bioeffects problems.

First, in Chapter 3 we present past work in which we simulate ultrasonically induced cavitation of contrast agent microbubbles in soft tissue (Patterson *et al.*, 2012). We use experimentally measured 1.5 – 7.5 MHz US waves, previously used by Miller *et al.* (2008) to determine kidney capillary hemorrhage threshold amplitudes in rats, as input to the simulation. The calculated cavitation dynamics and theoretical inertial cavitation thresholds (Flynn, 1982; Apfel, 1982) are compared with known thresholds for kidney hemorrhage to investigate their dependence on US, gas, and tissue properties. At the time of its publication, this work was unique in its combination of experimental results and numerical modeling to approach this problem.

Second, in Chapter 4 we present current work investigating a previously unconsidered potential mechanism for DUS-induced LH. We develop a model of DUS-alveolus interaction as an acoustically accelerated interface between two compressible fluids and perform numerical simulations to show that acoustically generated baroclinic torque at tissue-air interfaces within the lungs may be capable of deforming the fragile alveolar walls within the lungs, possibly to the point of hemorrhage. We generalize our discussion to acoustically-accelerated, perturbed, liquid-gas interfaces. Finally we propose future work to be completed for this dissertation.

CHAPTER 3

Past work: Theoretical microbubble Dynamics at capillary breaching thresholds

3.1 Abstract

In order to predict bioeffects in contrast-enhanced diagnostic and therapeutic ultrasound procedures, the dynamics of cavitation microbubbles in viscoelastic media must be determined. For this theoretical study, measured 1.5-7.5 MHz pulse pressure waveforms, which were used in experimental determinations of capillary breaching thresholds for contrast-enhanced diagnostic ultrasound in rat kidney, were used to calculate cavitation nucleated from contrast agent microbubbles. A numerical model for cavitation in tissue was developed based on the Keller-Miksis equation (a compressible extension of the Rayleigh-Plesset equation for spherical bubble dynamics), with a Kelvin-Voigt constitutive relation. From this model, the bubble dynamics corresponding to the experimentally obtained capillary breaching thresholds were determined. Values of the maximum radius and temperature corresponding to previously determined bioeffect thresholds were computed for a range of ultrasound pulses and bubble sizes for comparison to inertial cavitation threshold criteria. The results were dependent on frequency, the gas contents, and the tissue elastic properties. The bioeffects thresholds were above previously determined inertial cavitation thresholds, even for the tissue models, suggesting the possibility of a more complex dosimetry for capillary injury in tissue.

This work is has been published as

Patterson, B., Miller, D. L., & Johnsen, E. (2012). Theoretical microbubble dynamics in a viscoelastic medium at capillary breaching thresholds. *The Journal of the Acoustical Society of America*, 132(6), 3770. <http://doi.org/10.1121/1.4763993>

CHAPTER 4

Current work: Diagnostic Ultrasound Induced Lung Hemorrhage

4.0.1 Abstract

Over the past few decades, Diagnostic Ultrasound (DUS) of the lung has been shown to cause hemorrhage in a variety of mammals, though the underlying damage mechanism is yet to be determined. While there do not appear to be serious health risks associated with this problem under typical clinical conditions, the use of DUS for imaging of the lung is increasing rapidly. It is important we understand this phenomena to ensure that lung DUS remains safe as new procedures and technologies are developed. In this work we investigate the underlying physics associated with acoustic waves and liquid-gas interfaces and propose a previously unconsidered physical damage mechanism for DUS-induced Lung hemorrhage (LH). Specifically we propose that misalignments between ultrasound pressure gradients and tissue-air interface density gradients result in the generation of baroclinic vorticity, which could drive fragile cellular barriers around the alveoli to deform and ultimately hemorrhage. To investigate our hypothesis, we treat the lung as an inviscid, compressible fluid system and develop a simplified, numerical model of the problem to simulate DUS pulse-alveolus interaction. We show that acoustic waves, such as DUS pulses, are capable of generating baroclinic vorticity at sharp liquid-gas interfaces such as those found in the lungs, and that this drives subsequent deformation of the interface. We perform analysis to describe the vorticity and interface dynamics and propose a scaling law based on dimensional analysis to predict the growth of a purely circulation driven interface. We compare predicted results with numerical experiments to verify that baroclinic vorticity is the mechanism responsible for the deformation.

Finally we suggest future work to be completed for this dissertation in the upcoming year. We plan to increase the relevance of this work to lung Ultrasound (US) by using more realistic geometries and computing theoretical stresses within the lungs. Additionally we will model the circulation and interface deformation associated with simple expansion and compression waves and use these models to design optimal waveforms for minimizing interface growth after the passage of the wave.

4.1 Introduction

4.1.1 A review of previous work on diagnostic ultrasound-induced lung hemorrhage

DUS is the safest form of medical imaging available today and has become ubiquitous in clinical practice. Currently, the only known bioeffect of non-contrast DUS known to occur in mammals is LH. The physical damage mechanisms underlying, DUS-induced LH are presently unknown, though the damage does not appear to be particularly severe, and is not considered a problem of significant clinical concern. However, it is an important problem to understand if we hope to improve lung DUS by expanding the US regimes used in clinical application. In this work, we use numerical experiments to investigate the underlying physics of DUS wave-lung interaction. We model the lung as a compressible multi-fluid system and solve the Euler equations of inviscid fluid motion to study the dynamics of fluid-fluid interfaces exposed to

acoustic waves relevant to DUS. We observe that acoustically-generated vorticity at perturbed water-air interfaces drives the interface to deform. We hypothesize that a similar mechanism may be responsible for deforming and ultimately rupturing the fragile tissue barriers around alveoli, tiny air sacs within the lungs, leading to DUS induced LH.

US-induced LH is not a new problem. It was first discovered in mice over 20 year ago (Child *et al.*, 1990). Since then, the use of lung DUS has become increasingly common in certain critical care situations (Lichtenstein, 2009). And there has been much work to better understand the problem of DUS-induced LH. Previous research has primarily aimed at three specific ends: (1) Determining the dependence of damage characteristics and thresholds on the characteristics of the US subject; (2) Determining the dependence of damage characteristics and thresholds on the US properties; and (3) Investigating the physical damage mechanism causing the hemorrhage. Our work aims to contribute to this third area by investigating the fundamental physics underlying the problem.

Work in the first area has considered species, age, physiological development, and pulmonary state of the US subject as possible variables which DUS-induced LH may depend upon. Within mammals, DUS-induced LH has been observed to be largely species indiscriminate and has been found to occur in mice, pigs, rats, rabbits, and monkeys (Baggs *et al.*, 1996; Child *et al.*, 1990; Dalecki *et al.*, 1997; Frizzell *et al.*, 1994, 2003; Harrison *et al.*, 1995; Holland *et al.*, 1996; Kramer *et al.*, 2001; O'Brien & Zachary, 1997; O'Brien *et al.*, 2001a, 2003a, 2005, 2000, 2001c; Penney *et al.*, 1993; Raeman *et al.*, 1993, 1996; Tarantal & Canfield, 1994; Zachary & O'Brien, 1995; Zachary *et al.*, 2001a,b). Dalecki *et al.* (1997) investigated the effect of age on DUS-induced LH in mice by exposing neonatal, juvenile, and adult mice to DUS pulses. The study found that while hemorrhage thresholds were similar in all mice, the degree of hemorrhage was much greater in the adult mice than in the younger subjects. Similarly, O'Brien *et al.* (2003a), studied the age dependence of hemorrhage in pigs, and found that older pigs had a significantly lower hemorrhage thresholds than juvenile and middle-aged pigs. In an unexpected result, the study also found that if one lung was exposed to US and the pig was then rolled over and the second lung exposed, the hemorrhage threshold in the second lung was substantially lower than in the first. In a separate study, O'Brien *et al.* (2002) subjected rats with variable degrees of lung inflation to DUS in order to study the role of the impedance boundary condition at the lungs pleural surface on LH. It was found that rats with deflated lungs, that had less impedance mismatch with their surroundings, were more easily damaged than inflated lungs. While no direct experimentation has been performed on humans, for obvious ethical reasons, Meltzer *et al.* (1998) found that transesophageal echocardiography with similar US parameters to those causing lung hemorrhage did not lead to visible hemorrhage on the surface of the lung. While DUS-induced LH has not been shown to occur in humans, it has been demonstrated in a wide variety of mammals of varying age and size. The work presented here is not specific to any particular species or subject, but aims to consider the more general physical problem at hand.

The second area of research, investigating the dependence of lung hemorrhage on US properties, has seen the largest amount of work and is important for designing US in a way that is capable of high quality diagnostic imaging while minimizing any unwanted bioeffects. Research in this area has looked at the dependence of hemorrhage on US waveform and dosimetric properties. Zachary & O'Brien (1995) used continuous-wave and pulsed-wave US in mice, rabbits, and pigs, and found that while the continuous- and pulsed-wave-induced lesions appear macroscopically similar, they differ microscopically. Hemorrhage induced by continuous wave US consisted primarily of plasma and contained some cells, whereas pulsed-wave induced hemorrhage was composed largely of cells and contained little plasma. Raeman *et al.* (1996) subjected mice to pulsed US with varying exposure time and concluded that while threshold amplitudes appeared insensitive to exposure time, suprathreshold damage increased with increasing exposure. O'Brien *et al.* (2001b) investigated the effects of US beamwidth and found that as beamwidth increased so did the incidence, surface area, and volume of hemorrhage. It was noted that lung hemorrhage is perhaps

the only known beamwidth-dependent mechanical bioeffect of US. O'Brien *et al.* (2003b) found evidence that increasing US pulse duration increases the likelihood of lung hemorrhage in rats. In this effort we consider the dependence of the alveolar wall dynamics on acoustic properties relevant to US, including acoustic wave amplitude, duration, and pressure gradient, which we relate back to US more closely in our discussion of our results (See Section 4.4.3).

While work in the third area of research, studying the cause of DUS-induced LH, has not yet led to a conclusive determination of the specific physical damage mechanisms, the most common ultrasound bioeffects mechanisms have been shown to be unlikely causes of the damage. Zachary *et al.* (2006) found that DUS-induced lung lesions do not appear similar to those induced by heat, and hence concluded that thermal damage mechanisms are unlikely. O'Brien *et al.* (2000) observed that the severity of DUS-induced LH in mice increased under raised hydrostatic pressure. And Raeman *et al.* (1996) notes that hemorrhage is unaffected by the introduction of US contrast agents into subjects. Both of these findings suggest that Inertial Cavitation (IC) is not a likely cause of DUS-induced LH. However, Holland *et al.* (1996) reports detecting cavitation during DUS-lung interaction in rats. Tjan & Phillips (2007, 2008) model DUS of the lung as an inviscid, free surface subjected to a Gaussian velocity potential and perform simulations to find that this setup can lead to the ejection of liquid droplets. They go on to say that DUS of the lung may similarly lead to ejected droplets capable of puncturing the air-filled sacs within the lung. Despite these efforts, the precise damage mechanism underlying DUS-induced LH is still unknown. In this work we propose a previously unconsidered mechanical damage mechanism and perform simulations to investigate its feasibility.

4.1.2 A review of previous work on driven fluid-fluid interfaces

Within the fluids community, there has been extensive research into the fundamental physics describing interactions between mechanical waves and fluid interfaces. Much of this research is motivated by applications in fusion energy and astrophysics and accordingly has investigated the Richtmyer-Meshkov Instability (RMI), in which a perturbed fluid-fluid interface is accelerated by a shock, causing the interface perturbation to grow (Brouillette, 2002; Drake, 2006). The growth is driven by a sheet of baroclinic vorticity deposited along the interface as a result of misalignment between the pressure gradient across the shock and the density gradient across the perturbed interface. This physical mechanism by which these misaligned gradients create a torque on fluid particles and generate vorticity can be thought of in terms of a hydrostatic balance upon a particle. Pressure gradients result in acceleration of the flow. This acceleration is inversely proportional to density, resulting in shear and vorticity Heifetz & Mak (2015). This is illustrated in Figure 4.1. The existence of baroclinic vorticity can be shown by taking the curl of the conservation of momentum equation for a compressible fluid, however we note that it is a nonlinear effect cannot be explained by traditional linear acoustics. 4.1 from Heifetz & Mak (2015).

For the classical RMI setup, a planar shock impinges normally upon the peaks and troughs of a sinusoidal interface. As the degree of misalignment varies along the interface, the interface is accelerated non-uniformly. The direction of the vorticity changes where the slope of the interface changes. This counter rotation on either side of interface peaks and troughs entrains nearby fluid causing interface peaks to accelerate in one direction and troughs to accelerate in the opposite direction. This results in a “bubble” of light fluid penetrating the heavy fluid, and a “spike” of heavy fluid penetrating the light fluid. How exactly this occurs varies slightly depending on the relative densities of the two fluids. For the case of a wave moving from a light fluid into a heavy one, the peaks and troughs of the interface are initially accelerated to move away from one another, and the interface perturbation amplitude undergoes growth exclusively. For the case of a wave moving from a heavy fluid to a lighter fluid, the peaks and troughs of the interface are accelerated such that they initially move closer to one another decreasing the perturbation amplitude.

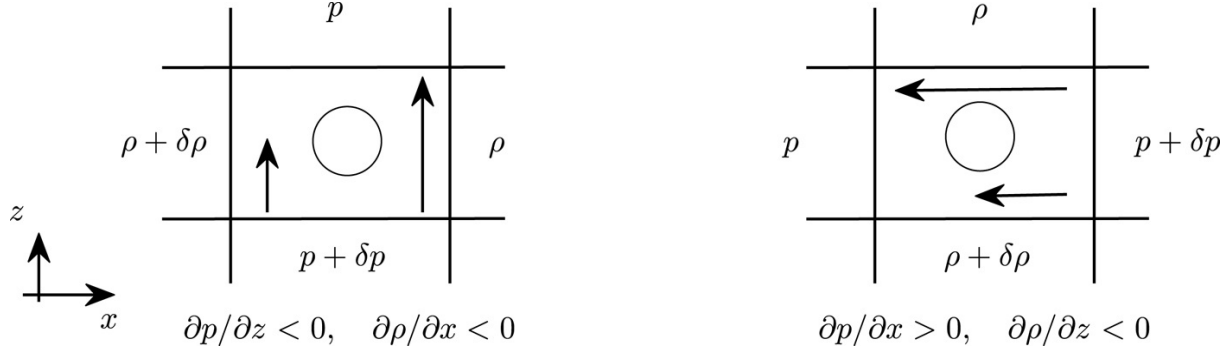


Figure 4.1: From Heifetz & Mak (2015). A hydrostatic force balance upon a particle subject to perpendicular pressure and density gradients illustrates baroclinic torque on a fluid particle.

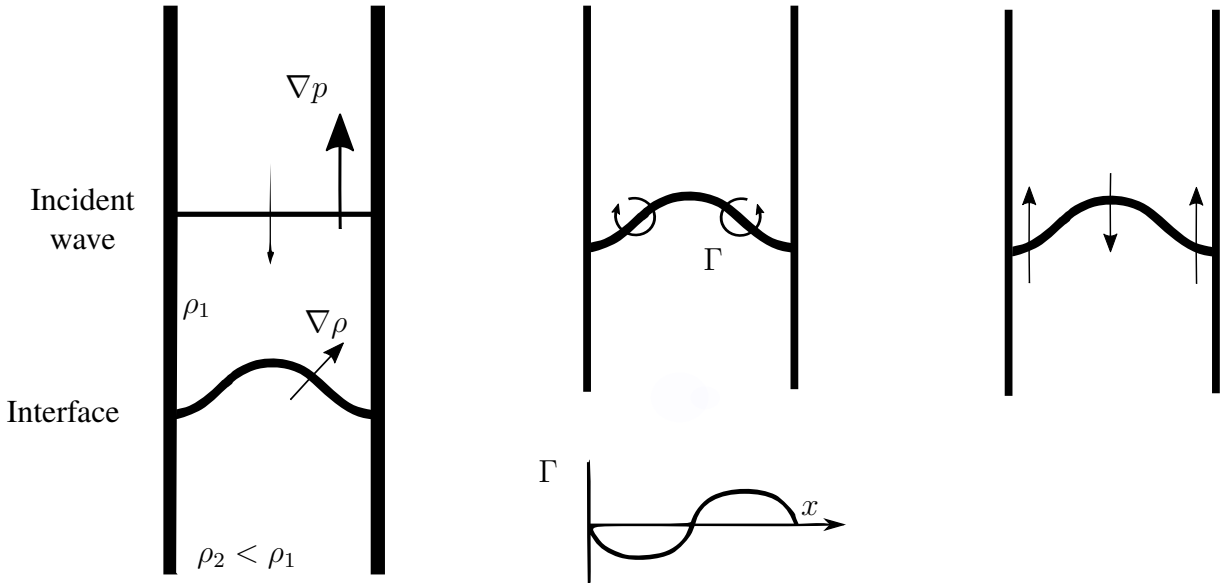


Figure 4.2: Adapted from Brouillette (2002). The RMI for a heavy-light interface is illustrated. The initial condition (left), circulation post wave-interface interaction (center), and perturbation growth (right) are shown.

They then pass one another, inverting the phase of the interface perturbation, and then continue moving in opposite directions, growing the perturbation amplitude. This process is illustrated in Figure 4.2, which has been adapted from Brouillette (2002).

Previous studies of the RMI have utilized theory, computation, and experiments to describe the behavior of the interface after the wave has passed. Richtmyer (1960) performed the linear stability perturbation analysis developed by Taylor (1950) for the case of an impulsive acceleration to create a model for the initial growth of the interface perturbation. Meshkov (1972) experimentally confirmed Richtmyer's qualitative predictions, hence the name of the instability. Meyer (1972) performed numerical simulations of the RMI and found good agreement with Richtmyer for the case of a shock impinging upon a light-heavy interface. Fraley (1986) used Laplace transforms in order to find the first analytical solution for the asymptotic growth rate for a shocked interface between perfect gases. To describe the late time, nonlinear growth of the perturbation, Zhang & Sohn (1997) used single mode perturbation, keeping many high order terms, to describe the velocity of the bubble and spike regions of the fluid. Sadot *et al.* (1998) combined the linear, impulsive solution with potential flow models of the asymptotic behavior of the bubble and spike

to develop a model for the perturbation growth that is in good agreement with shock tube experiments for shocks with Mach numbers $\text{Ma}=1.3, 3.5$. Vortex theory has also been used to describe the behavior of the interface. [Jacobs & Sheeley \(1996\)](#) horizontally oscillated a container with two vertically stratified liquids to obtain standing waves and then bounced the container off of a coil spring to study the incompressible RMI. The late time evolution of the interface is modeled using a row of line vortices to obtain qualitatively similar results to those experimentally observed, however the late-time growth rate is underestimated. [Samtaney & Zabusky \(1994\)](#) used shock polar analysis to find the circulation deposited by a shock on planar and non-planar interfaces. Their results are validated using an Euler code and found to be within 10% of the computed value for $1.0 < \text{Ma} \leq 1.32$ for all $\rho_2/\rho_1 > 1$, and $5.8 \leq \rho_2/\rho_1 \leq 32.6$ for all Ma . This work aims to add to the current body of work on this topic by investigating interfaces accelerated by pressure waves within the acoustic regime.

4.1.3 Explanation and contributions of the present work

We argue that the basic problem setup of the RMI, a mechanical wave impinging upon a material interface, is similar to DUS of the lungs. Accordingly we propose another possible damage mechanism of DUS-induced LH. We hypothesize that misalignment between the pressure gradients in the DUS pulses and the sharp density gradients across the tissue-air interfaces of the lungs creates a torque around the alveoli, which deforms and ultimately hemorrhages the alveolar walls.

The detailed nonlinear interactions between acoustic waves and perturbed fluid-fluid interfaces does not appear to have been previously studied in this manner or context. This work is separate from previous research into the RMI as a result of the acoustic waves being studied. Unlike shock waves, which occur over a few molecular mean free paths and interact nearly instantaneously, acoustic waves have a finite spacial wavelength and can occupy a much larger portion of space. Consequently, their interaction with interfaces occurs over a longer period of time, the duration of which depends on a variety of factors including shape and amplitude of the waveform, the speed of sound in the media, the relative orientation of the traveling wave and the interface (e.g., the shape of the interface). This duration can also be thought of in terms of the relative sizes of the physical features of the interface and the wavelengths of each feature of the acoustic wave of interest. Simple RMI analysis assumes an impulsive acceleration, and does not apply to this work because the interface has time to deform throughout its interaction with the wave. In this work we demonstrate that the finite duration of the wave-interface interaction can effect the qualitative behavior of the interface dynamics because of the interface deformation that occurs during this period. We will specifically attempt to address the following questions:

1. Are acoustic waves capable of generating sufficient baroclinic vorticity at perturbed fluid-fluid interfaces for substantial deformations?
2. what is the impact of the acoustic wave properties, such as amplitude and wave duration, on the vorticity and interface dynamics?

In the remainder of this work, we will first present a simplified model problem and a set of numerical experiments designed to investigate the fundamental physics underlying interactions between acoustic waves and perturbed interfaces between fluids. The simulation results and related analysis will be presented and discussed first in the context of the fluid dynamics. We will then draw from these results to further elaborate on the significance of these results as they regard to the motivating problem of DUS-induced lung hemorrhage. We will finally end by summarizing the main conclusions drawn from this work and suggest the next steps to be taken.

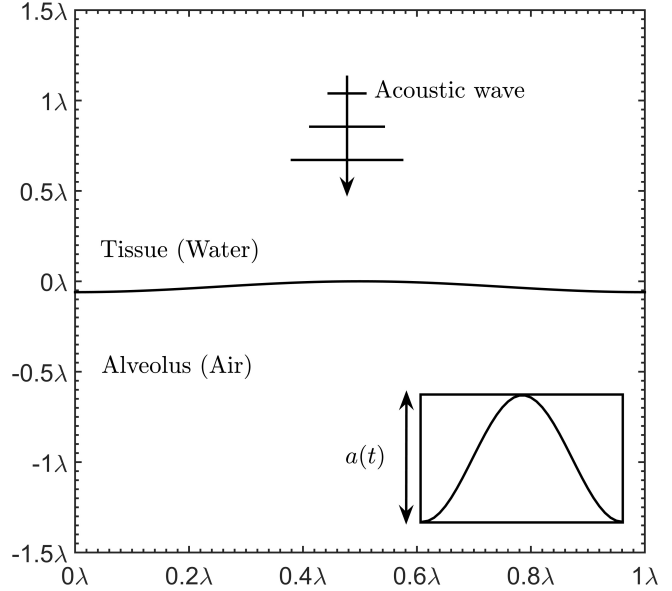
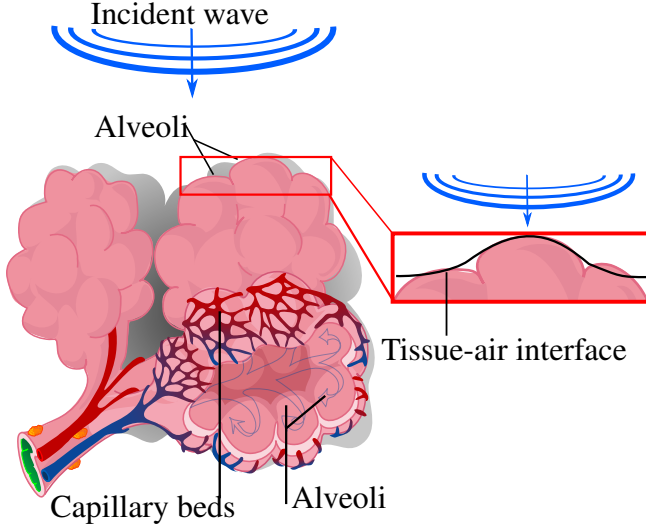


Figure 4.3: A schematic view of the physical problem (left) is shown next to a schematic view of initial setup and boundary conditions of the numerical experiments performed (right). A DUS pulse impinging from tissue onto a pulmonary alveolus is modeled as an acoustic wave impinging from water onto a sinusoidally perturbed water-air interface.

4.2 Methods

In this section, we describe the set of numerical experiments performed to investigate the fundamental fluid dynamics associated with acoustically-accelerated, perturbed liquid-gas interfaces and US-induced LH.

4.2.1 Problem set-up

The experiments are designed to model the physics associated with a DUS pulse propagating from soft lung tissue (modeled as water) onto a pulmonary alveolus (modeled as air). Accordingly, we consider a 2D, compressible inviscid fluid system in the xy -plane with an acoustic wave impinging from water (top) downward toward air (bottom). The water-air interface is initially located near $y = 0$ and has a sinusoidal shape with wavelength λ and amplitude 0.03λ as seen in Figure 4.3. The width of the rectangular computational domain is 1λ such that it is traversed by a single period of the interface. This interface geometry is consistent previous studies of the RMI (Brouillette, 2002).

To model the DUS pulse we consider two different waveforms with different purposes. We design the first waveform to closely resemble a typical DUS pulse, in order to simulate the appropriate dynamics. The waveform shape is composed of a sinusoidal pressure modulated by a Gaussian envelope as seen in Figure 4.4),

$$p(t) = p_a \sin(2\pi f [(t - t_0)^2]) \exp\left(-\frac{t - t_0}{FWHM / (2\sqrt{2 \ln(2)})}\right). \quad (4.1)$$

Here $p(t)$ is the pulse pressure as a function of time, p_a is the maximum acoustic pressure, f is the frequency in Hz, t is time, t_0 is a time offset, and $FWHM$ is the full width at half maximum amplitude

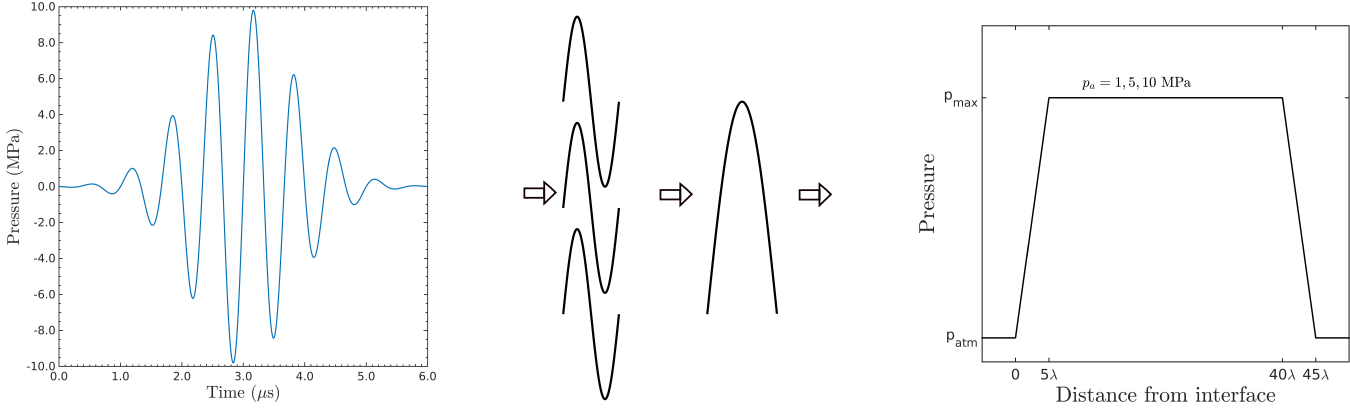


Figure 4.4: The initial pressure waveforms in the domain. A DUS pulse used as in initial condition (Left) is thought of as a sum of (half) sinusoids (Center), which can each be approximated as a trapezoidal waves (Right). The trapezoidal wave initial condition, shown as a function of vertical distance from the interface, is used for the bulk of this study.

for the Gaussian envelope. The presented DUS- pulse waveform is given as a function of time, as is typical of US. The speed of sound in water is used to convert this to a spatial waveform for the initial condition.

Because A typical DUS pulse is mathematically complicated and not ideal for analysis we also use a trapezoidal waveform, which is sufficiently simple such that the relevant vorticity and interface dynamics can be studied analytically. To design this wave, we think of the ultrasound pulse as a sum of sin waves, each of which is composed of half-sinusoids, which can be approximated as trapezoidal waves. This thought process is illustrated in figure 4.4 (Left). Hence we use an initially symmetric trapezoidal waves.

Each wave is prescribed as an initial condition in the flow and is composed of three stages, described here in the order that they encounter the interface. First, compression occurs. Pressure increases linearly from atmospheric to a maximum of $p_a = 1, 5$, or 10 MPa gauge pressure. Second, the elevated pressure p_a remains constant over a fixed distance (or time). Third, expansion occurs and pressure decreases linearly back to atmospheric pressure. The pressure rise and fall occur over equal distances 5λ , such that they have constant, equal slopes $\pm p_a/5\lambda$. Note that this neglects wave distortion due to acoustically induced changes in sound speed, which we assume to be small for our purposes. Unless otherwise stated, the period of constant pressure has length 35λ . Hence the total length L of the incoming trapezoidal wave is 45λ . We assume a typical alveolar length scale $\lambda = 100 \mu\text{m}$. For the wave initially in water, ($c=1500 \text{ m/s}$), we find an equivalent acoustic pulse duration of our waveform is $3 \mu\text{s}$. This is within the range of typical US pulse durations in clinical imaging (Edelman, 2005) and relevant research (O'Brien, William D. *et al.*, 2006).

4.2.2 Governing equations

The governing equations describing the dynamics US lung interaction are conservation of mass, momentum, and energy for a compressible, viscoelastic material. In the present work we neglect elastic and viscous effects to arrive at the Euler equations of fluid motion, which we nondimensionalize by the density ρ and speed of sound c of air. For our setup we model the tissue as water and alveolus as air and the DUS pulse as a trapezoidal pressure waveform. Hence we solve the Euler equations to simulate simplified trapezoidal acoustic waves propagating from water towards a sinusoidally perturbed water-air interface. The interface and vorticity dynamics are studied.

It is worth noting that the Euler equations are length scale invariant, and thus no inherent physical length scale exists in the equations that we solve. Hence all length scales hereafter will be considered

relative to an interface perturbation wavelength λ . Within the context of the DUS, λ can be thought of as a typical length scale of an alveolus.

We solve the dimensionless Euler equations of compressible, inviscid fluid motion in two dimensions (x, y) ,

$$\frac{\partial \rho}{\partial t} + \frac{\partial (\rho u)}{\partial x} + \frac{\partial (\rho v)}{\partial y} = 0, \quad (4.2a)$$

$$\frac{\partial \rho u}{\partial t} + \frac{\partial}{\partial x} (\rho u^2 + p) + \frac{\partial}{\partial y} (\rho u v) = 0, \quad (4.2b)$$

$$\frac{\partial \rho v}{\partial t} + \frac{\partial}{\partial x} (\rho u v) + \frac{\partial}{\partial y} (\rho v^2 + p) = 0, \quad (4.2c)$$

$$\frac{\partial E}{\partial t} + \frac{\partial}{\partial x} [u(E + p)] + \frac{\partial}{\partial y} [v(E + p)] = 0, \quad (4.2d)$$

where t is time, ρ is density, p is the pressure, u and v are the velocity components in the x and y directions respectively, and E is the total energy. We use the density and sound speed of air at 300 K to nondimensionalize the system. It is worth noting that the Euler equations are length scale invariant, and thus no inherent physical length scale exists in the equations that we solve. Hence all length scales hereafter will be considered relative to an interface perturbation wavelength λ .

To close the system, we solve a stiffened equation of state which relate the total energy to the pressure and velocity in the flow, such that,

$$E = \frac{\rho(u^2 + v^2)}{2} + \frac{p + \gamma B}{\gamma - 1}. \quad (4.3)$$

Here B is a measure of liquid stiffness. For perfect gases, such as is our treatment of air, γ is the specific heats ratio and $B = 0$. The sound speed in our simulations is calculated based on the following relationship, derived from the stiffened equation of state.

$$c = \sqrt{\frac{\gamma(p + B)}{\rho}}. \quad (4.4)$$

While physical diffusion is not considered in this setup, numerical diffusion does occur at the water-air interface, creating a mixed region between the two fluids. The numerical treatment of the diffusion layer at the interface for the initial condition is such that the density has an exponential profile ([Latini et al., 2007](#)), which is used to get the mass fraction and molecular weight fields in the mixed region. Which then used to determine the other material parameters in the mixed region in a thermodynamically consistent fashion.

To solve for the material parameters in the mixed region and prevent spurious pressure oscillations at the interface, two additional advection equations are solved for γ and B .

$$\frac{\partial}{\partial t} \left(\frac{\gamma B}{\gamma - 1} \right) + \vec{u} \frac{\partial}{\partial x} \left(\frac{\gamma B}{\gamma - 1} \right) = 0, \quad (4.5a)$$

$$\frac{\partial}{\partial t} \left(\frac{1}{\gamma - 1} \right) + \vec{u} \frac{\partial}{\partial x} \left(\frac{1}{\gamma - 1} \right) = 0. \quad (4.5b)$$

This implementation is consistent with the works of [Abgrall \(1996\)](#); [Shyue \(2001\)](#); [Alahyari Beig & Johnsen \(2015\)](#). Details of this implementation are explained by [Henry de Frahan et al. \(2015\)](#). The dimensional and dimensionless values of each fluid property can be found in tables 4.1 and 4.2 respectively.

4.2.3 Numerical methods

To solve the governing equations, we implement a third-order accurate Discontinuous Galerkin (DG) scheme in space and a fourth-order accurate, adaptive Runge-Kutta method to march forward in time ([Henry de Frahan et al., 2015](#)). Roe solver is used to calculate flux in an out of each cell in a way that handles discontinuities and keeps the interface sharp. As previously stated, the computational domain width (x -direction) is λ . The domain length (y -direction) is 80λ . The grid resolution is 100 points per λ unless otherwise stated. To minimize artificial reflections, we use inflow and outflow boundary conditions at the top and bottom of the domain, and implement geometric grid stretching in the vertical direction for the top and bottom-most 10λ segments of the grid. Periodic boundary conditions are used at the left and right edges of the domain.

4.3 Analysis

We perform analysis to make quantifiable predictions about the vorticity and interface dynamics. The results of these analyses are compared with the results of our numerical experiments in section 4.4.

To better understand the source of circulation within our problem we look to the vorticity generation equation for a 2D, inviscid fluid system,

$$\frac{\partial \vec{\omega}}{\partial t} + (\vec{u} \cdot \nabla) \vec{\omega} = -\vec{\omega} (\nabla \cdot \vec{u}) + \frac{\nabla \rho \times \nabla p}{\rho^2}. \quad (4.6)$$

Each term in equation (4.6) represents a different physical mechanism by which the vorticity $\vec{\omega}$ is changing. The terms on the left-hand side of the equation represent changes in the existing vorticity field and the terms on the right represent vorticity sources and sinks. The first term on the left represents the total change of vorticity at a location in the flow field with respect to time. The second term on the left represents the advection of vorticity within the field. The first term on the right describes changes in vorticity due to compressibility. The last term on the right is the baroclinic term which represents vorticity generated by the misalignment of the pressure and density gradients in the flow. We seek to understand the relative importance of these mechanisms on the dynamics of the acoustically driven interface.

4.3.1 Order of magnitude analysis of vorticity generation mechanisms

To quantifiably compare the various mechanisms by which vorticity changes within the flow, we recognize that any vorticity generated must be a result of acoustic energy being converted to kinetic energy. As the only mechanism for this to occur in an inviscid fluid without pre-existing vorticity is baroclinic, we require misaligned density and pressure gradients. Hence we choose to perform our analysis at the water-air interface during the period in which the interface is interacting with the incoming wave. For simplicity,

Table 4.1: Dimensional properties of air and water used in simulations.

	Density, ρ^* (kg/m ³)	γ	B^* (Pa)	c^* (m/s) ($p=1$ atm)
Air	1.18	1.4	0	347.2
Water	996	5.5	492115000	1648.7

* indicates dimensional parameter

we narrow this down to only consider the period in which the incoming compressive portion of the wave encounters the interface. As this interaction occurs quickly, over an approximate time span $\Delta t_a \approx 5\lambda/c_w$, we assume that the interface is static and remains undeformed from its initial state during this interaction. We will show in section 4.4 that this assumption is reasonable for the cases considered. Having now established the point at which the analysis is to be performed we evaluate the order of magnitude of the compressible, advective, and baroclinic terms of the vorticity generation equation (4.6). We note that the advective term is not a true source of vorticity, but is useful in understanding the change of vorticity at a given time and location within the flow.

In our evaluation of the order of magnitude of the individual terms of the vorticity generation equation (4.6), we treat gradient, curl, and divergence terms of any arbitrary quantity f such that $\nabla f = \mathcal{O}(|\Delta f|/\Delta L)$, $\nabla \cdot f = \mathcal{O}(|\Delta f|/\Delta L)$, and $\nabla \times f = \mathcal{O}(|\Delta f|/\Delta L)$. Here Δf is a change in f over a characteristic length scale ΔL . Because the only motion in the flow is generated by the acoustic wave. Accordingly, we consider acoustic pressure, velocity, and density perturbations such that $\Delta p = \Delta p_a$, $\Delta \vec{u} = \Delta \vec{u}_a$, and $\Delta \rho = \Delta \rho_a$, and use acoustic relations to relate these quantities (Anderson, 1990),

$$\Delta p_a = \pm \Delta u_a \rho c = c^2 \Delta \rho_a. \quad (4.7)$$

Additionally, to evaluate the expressions in this section we use the values in tables 4.1 and 4.2 consider our base trapezoidal wave case where $p_a = \Delta p_a = 10$ MPa. The length scale associated with the acoustic wave is the initial length of the pressure rise $\Delta L_a = 5\lambda$. The initial interface length scale ΔL_I , defined as the thickness of the mixed gas-liquid region of the interface from volume fraction of water $y_0 = 0.05$ to 0.95 volume fraction is estimated as $\Delta L_I \approx 0.05\lambda$. We approximate the order of theta based on its average value along a half-wavelength of the interface for our initial condition $a_0 = 0.03\lambda$ such that $\overline{|\theta|} \approx 0.12$.

To assess the baroclinic contribution to vorticity, we write the cross product of the density and pressure gradients as $|\nabla \rho| |\nabla p| \sin(\theta)$. Here θ is the angle between the acoustic pressure gradient, treated as constant in the $+y$ -direction, and the direction of the density gradient which we treat as the outward normal direction to the interface. For $a_0/\lambda \ll 1$, we can approximate $\sin(\theta) \approx \theta$ at the interface. The density gradient due to the water-air interface is far greater than that due to the acoustic wave. As such we use the change in density across the interface $\Delta \rho_I$ and associated length scale ΔL_I to write the density gradient. The pressure change is a result of the acoustic wave, and as such we use the acoustic pressure change Δp_a and associated length scale ΔL_a to express the pressure gradient. And thus we write the order of magnitude of the baroclinic vorticity generation term at the interface,

$$\left| \frac{\nabla \rho \times \nabla p}{\rho^2} \right| = \mathcal{O} \left(\frac{|\Delta \rho_I|}{|\Delta L_I|} \frac{|\Delta p_a|}{|\Delta L_a|} \frac{1}{|\rho|^2} |\theta| \right). \quad (4.8)$$

In the evaluation of the compressible and advective terms we consider two possible cases for the evaluation of the vorticity, based on whether the dominant vorticity arises from the acoustic flow-field or is baroclinically generated. Thus we will ultimately treat $\vec{\omega}$ as either the curl of the acoustic velocity field $\vec{\omega} = \nabla \times \vec{u}$ or the integral of the baroclinic vorticity generation term (4.8), treated as constant, over the characteristic time of the pressure rise $\Delta t_a \approx \Delta L_a/c_w$.

Table 4.2: Dimensionless properties of air and water used in simulations.

	Density, ρ	γ	B	c
Air	1	1.4	0	1
Water	846.6	5.5	3469.1	4.75

Parameters are nondimensionalized by the density and sound speed of air.

We first consider the case in which vorticity is predominately a product of the acoustic velocity field such that the approximate order of magnitude of the compressible contribution to vorticity generation is expressed as

$$|-\vec{\omega}(\nabla \cdot \vec{u})| = \mathcal{O}\left(\left[\frac{|\Delta u_a|}{|\Delta L_a|}\right]^2\right), \quad (4.9)$$

and for the advective contribution we find

$$|(\vec{u} \cdot \nabla) \vec{\omega}| = \mathcal{O}\left(\left[\frac{|\Delta u_a|}{|\Delta L_a|}\right]^2\right). \quad (4.10)$$

We note that from this analysis, we expect the advective and compressible vorticity effects to be of the same order during considered period and will treat them as such for the remaining analysis.

Now, to compare the relative importance of the baroclinic and compressible (or advective) contributions to vorticity for this case we will look at the ratio of the two vorticity generation approximations. We divide equation (4.8) by equation (4.9) use (4.7) to express acoustic quantities in terms of the density perturbation $\Delta\rho_a$ and simplify,

$$\begin{aligned} \frac{\left|\frac{\nabla\rho \times \nabla p}{\rho^2}\right|}{|-\vec{\omega}(\nabla \cdot \vec{u})|} &= \mathcal{O}\left(\left(\frac{|\Delta\rho_I|}{|\Delta L_I|} \frac{|\Delta p_a|}{|\Delta L_a|} \frac{1}{|\rho|^2} |\theta|\right) / \left(\left[\frac{|\Delta u_a|}{|\Delta L_a|}\right]^2\right)\right) \\ &= \mathcal{O}\left(\left[\frac{|\Delta\rho_I|}{|\Delta L_I|} \frac{|\Delta\rho_a|}{|\Delta L_a|} \frac{|c|^2}{|\rho|^2} |\theta|\right] / \left[\frac{|c|}{|\rho|} \frac{|\Delta\rho_a|}{|\Delta L_a|}\right]^2\right) \\ &= \mathcal{O}\left(\frac{|\Delta\rho_I| / |\Delta L_I|}{|\Delta\rho_a| / |\Delta L_a|} |\theta|\right). \end{aligned} \quad (4.11)$$

Evaluating the right-hand side of (4.11) using the previously described approximations and values we find that the ratio of baroclinic vorticity and compressible contributions to vorticity to be of order $\mathcal{O}(10^3)$.

As the previous result would suggest that baroclinic vorticity generation is strongly dominant, we must check the result by again evaluating the compressible and advective contributions to vorticity generation, using an expression for vorticity based on the time integration of (4.8),

$$|-\vec{\omega}(\nabla \cdot \vec{u})| \sim |(\vec{u} \cdot \nabla) \vec{\omega}| = \mathcal{O}\left(\frac{|\Delta u_a|}{|\Delta L_a|} \frac{|\Delta\rho_I|}{|\Delta L_I|} \frac{|\Delta p_a|}{|\Delta L_a|} \frac{1}{|\rho|^2} |\theta| \frac{|c|}{|\Delta L_a|}\right). \quad (4.12)$$

Again, comparing the relative importance of the baroclinic and compressible (or advective) contributions to vorticity as we did before,

$$\frac{\left|\frac{\nabla\rho \times \nabla p}{\rho^2}\right|}{|-\vec{\omega}(\nabla \cdot \vec{u})|} = \frac{c}{|\Delta u_a|} = \frac{\rho}{|\Delta\rho_a|} \quad (4.13)$$

Now evaluating this expression we expect that the relative contribution of baroclinic to compressible/advective vorticity generation is approximately of order $\mathcal{O}(10^2)$ at the end of the compression-interface interaction.

Comparing the evaluations of expressions (4.11) and (4.13) we expect two things. First, that baroclinicity will be the dominant physical mechanism by which circulation is generated. Hence, we expect that (4.11) is likely to overestimate the dominance of baroclinic vorticity after a small amount of baroclinic vorticity has been generated. Second, we expect the ratio of the baroclinic to compressible contributions to vorticity generation will range from $\mathcal{O}(10^3)$ to $\mathcal{O}(10^2)$ during the compression-interface interaction.

4.3.2 Comparison of vorticity generation in air and water

Having established that the dominant source of vorticity is baroclinicity we now aim to determine where this vorticity will be generated within the mixed gas-liquid interface region. Specifically, we aim to compare the order of baroclinic vorticity generation from equation (4.8) in pure water and air. As this can already be evaluated in water from what we have provided up to this point, we will focus on evaluation of the order of baroclinic vorticity generation in air, from equation (4.8). Throughout the analysis we will denote the properties of the incoming wave and water with a subscript $-$, and the transmitted wave and air with a subscript $+$. For water, we will use the values for $\Delta\rho_I$, ΔL_I , $\Delta\rho_a$, ΔL_a and θ defined in the previous section based on our initial condition. Our treatment of the density gradient at the interface will remain unchanged for evaluation in air such that $\Delta\rho_I^- = \Delta\rho_I^+$ and $\Delta L_I^- = \Delta L_I^+$.

As a portion of the acoustic wave is transmitted into air, it undergoes several physical changes relative to the incident wave. To describe the properties of the transmitted wave in air we will borrow techniques from linear acoustics. To find the pressure change in the transmitted compression wave Δp_a^+ , we recognize that $a_0/\lambda \ll 1$ and treat the incoming wave as a plane wave impinging normally on a flat material interface such that $\Delta p_a^+ = T\Delta p_a^-$, where T is the acoustic transmission coefficient, $T = 2\rho^+c^+ / (\rho^+c^+ + \rho^-c^-)$ (Kinsler *et al.*, 1982). For our water-air interface $T \approx 4.97 \times 10^{-4}$. Because of the strong impedance mismatch between fluids, the acoustic wave is almost entirely reflected, decreasing the pressure gradient of the transmitted wave relative to the incident wave. Because of the drop in sound speed across the interface, the transmitted wave is compressed into a smaller physical area (i.e., the wavelength decreases) relative to the incoming wave, such that $\Delta L_a^+ = \Delta L_a^-(c^+/c^-)$. This effect increases the pressure gradient in the transmitted wave. To evaluate θ^+ , we utilize Snell's law which states that $c^- \sin(\theta^-) = c^+ \sin(\theta^+)$. Tedious, but simple geometric arguments can be used to show that because $a_0/\lambda \ll 1$ it is also true that $\theta^- \ll 1$. Thus we use the small angle approximation of sin to find that $\theta^+ \approx \theta^-(c^+/c^-)$. We note that this decreases the misalignment between the pressure and density gradients in air, and quantitatively approximately cancels the increase in pressure gradient due to the decrease in wavelength of the transmitted wave.

To determine where the vorticity will be generated at the interface, we consider equation (4.8) in air and water and write the ratio to find

$$\begin{aligned} \frac{\left| \frac{\nabla\rho \times \nabla p}{\rho^2} \right|_{air}}{\left| \frac{\nabla\rho \times \nabla p}{\rho^2} \right|_{water}} &= \mathcal{O} \left(\frac{\left[\frac{|\Delta\rho_I^+|}{|\Delta L_I^+|} \frac{|\Delta p_a^+|}{|\Delta L_a^+|} \frac{1}{|\rho^+|^2} |\theta^+| \right]}{\left[\frac{|\Delta\rho_I^-|}{|\Delta L_I^-|} \frac{(|\Delta p_a^-|/|T|)}{|\Delta L_a^-|(|c^+|/|c^-|)} \frac{1}{|\rho^-|^2} (|c^+|/|c^-|) |\theta^+| \right]} \right), \\ &= \mathcal{O} \left(|T| \left(\frac{|\rho^-|}{|\rho^+|} \right)^2 \right). \end{aligned} \quad (4.14)$$

For our water-air interface, we evaluate equation (4.14) to find that the ratio of baroclinic vorticity generation in air to that in water would be of order $\mathcal{O}(10^2)$. While this result considers vorticity generation in pure air and water, as opposed to the mixed fluid region relevant to this work, it provides a useful upper bound on the change we expect in the vorticity across the interface. Additionally, this result suggests that for the mixed water-air region, where the strongest density gradient exists, vorticity generation is likely to occur in areas with a lower volume fraction of water (i.e., gas-dominated fluid).

4.3.3 Considerations of circulation

In order to verify our analyses numerically we will consider not the vorticity generation, but rather the circulation and circulation generation as functions of time. As circulation is a global quantity of vorticity

integrated over a region, it is more practical to compare to our numerical experiments. The expressions previously obtained for estimates of vorticity generation can be integrated in space to obtain integral expressions for circulation generation. As the expressions derived were approximate and spatially independent, we expect that the approximate vorticity relationships found in this section can be extended to considerations of the circulation. For instance, based on the results of equation (4.13) we expect the baroclinic circulation generation in the left or right half-domain to be $\mathcal{O}(10^2)$ larger than the compressible and advective terms toward the end of interaction between the interface and the acoustic compression.

To access this, we integrate equation (4.6) over the half-domain, A_R , to get

$$\left(\frac{\partial \Gamma}{\partial t} \right)_{total} = \left(\frac{\partial \Gamma}{\partial t} \right)_{compressible} + \left(\frac{\partial \Gamma}{\partial t} \right)_{baroclinic} - \left(\frac{\partial \Gamma}{\partial t} \right)_{advective}, \quad (4.15)$$

Each term will be analyzed separately to determine the individual physical contributions to circulation. Here

$$\left(\frac{\partial \Gamma}{\partial t} \right)_{compressible} = - \int_{A_R} \vec{\omega} (\nabla \cdot \vec{u}) dA_R, \quad (4.15a)$$

$$\left(\frac{\partial \Gamma}{\partial t} \right)_{baroclinic} = + \int_{A_R} \frac{\nabla \rho \times \nabla p}{\rho^2} dA_R, \quad (4.15b)$$

$$\left(\frac{\partial \Gamma}{\partial t} \right)_{advective} = + \int_{A_R} (\vec{u} \cdot \nabla) \vec{\omega} dA_R. \quad (4.15c)$$

Finally, as we expect the interface growth to be purely circulation driven long after all waves have left the domain, we perform dimensional analysis to find a scaling law for the corresponding interface perturbation amplitude $a(t)$ as a function of circulation and time,

$$a(t) \sim \sqrt{\Gamma t}. \quad (4.16)$$

This proposed scaling law will be compared to the late time dynamics of the interface, after the acoustic wave has left the domain in Section 4.4.1.2.

4.4 Preliminary results and discussion

In this section we present the results of the numerical experiments and compare them to our analysis. We focus specifically on the vorticity/circulation and interface dynamics. We first investigate the response of the trapezoidal wave case in detail and then qualitatively compare this to results for the US pulse case.

4.4.1 Interface response to the $p_a = 10$ MPa trapezoidal wave

4.4.1.1 Qualitative behavior of the interface and vorticity

To provide a qualitative understanding of the underlying physics, we consider our reference case in which a $p_a = 10$ MPa trapezoidal wave (See Figure 4.4) impinges on the water-air interface. Nearly all of the acoustic energy is reflected back into the water as a tension wave due lower acoustic impedance of the second fluid. The transmitted compression wave is weakly focused due to the sound speed mismatch across the curved interface perturbation. These reflected and transmitted waves dissipate at the inflow and outflow boundaries.

To illustrate the evolution of the interface and vorticity fields, Figure 4.5 contains color plots of the density (Top) and vorticity (Bottom) fields at different instances in the flow's evolution. Areas of high density (i.e., water) are dark blue and areas of low density (i.e., air) are light-blue. On the vorticity contours, counterclockwise (positive) vorticity is red, and clockwise (negative) vorticity is blue. The purpose of the vorticity plots is only to show the location and direction of vorticity at each time. For sake of visualization, the range of the vorticity color scale changes at each time slice because the vorticity spreads over time. Hence the vorticity magnitudes are not shown here. Contours of $y_0 = 0.5$ volume fraction are indicated in black on both plots.

The initially smooth interface perturbation grows from a smooth sinusoid to a sharp spike at late time. At $t = 1$, the compression-interface interaction has nearly completed and the vorticity is heavily concentrated in the air such that 97% of the total circulation in the left or right half domain exists in fluid with volume fraction of water $y_0 < 0.5$. This is qualitatively consistent with our analysis . As time progresses, it can be seen that the vorticity disperses throughout the domain, but remains concentrated around the interface and the vertical center of the domain.

To more closely exam the interface and circulation dynamics associated with the compression wave-interface interaction, Figure 4.6 shows the early-time histories of the interface amplitude $a(t)$ and half-domain circulation Γ . t_{1-4} are the times at which the interface first encounters each features of the incoming wave: 1-pressure rise, 2-static elevated pressure, 3-pressure fall, and 4-return to ambient pressure. These points are denoted with black \times s along the curves in these figures and those hereafter. From $t_1 = 0^+$ to t_2 the compression wave encounters the interface. During this interaction the perturbation amplitude decreases, and the right half-domain circulation Γ rises sharply. At $t_2 \approx 1.1$, the pressure reaches its maximum amplitude, $p_a = 10$ MPa, and remains constant until t_3 . We note that at $a(t_{1-2})/a_0 \approx 0.96$, suggesting that the static interface assumption made in our vorticity generation order of magnitude analysis was reasonable. The interface amplitude continues to decrease and the half-domain circulation Γ stops its rapid growth and changes little during this static elevated pressure period, until the expansion wave hits at t_3 . At $t \approx 5.0$, the perturbation undergoes a phase inversion and begins to grow, as is observed for the heavy-light interface Richtmyer-Meshkov problem. At $t_3 \approx 8.5$ the expansion wave first hits the interface. The perturbation amplitude continues to grow, and Γ increases sharply again. At $t_4 \approx 9.7$ the acoustic wave has finished traversing the interface, and atmospheric pressure is resumed. The perturbation amplitude a_0 continues to grow long after the wave-interface interaction has finished.

4.4.1.2 Dependence on acoustic wave amplitude

To investigate the dependence of the dynamics on the trapezoidal wave amplitude, we compare results for $p_a = 1, 5$, and 10 MPa while keeping the initial lengths of the wave L and the rise and fall ΔL_a constant such that p_a scales linearly with the acoustic pressure gradient. Figure 4.7, illustrates the interface amplitude and p_a -normalized circulation histories for $t \leq 25$, during and shortly after the wave-interface interaction. Black \times s along the curves indicate t_{1-4} , described previously in Subsection . During the interaction between the interface and the compression wave, the rate at which the perturbation amplitude decreases is greater for higher amplitude waves. The circulation deposited during this period scales linearly with p_a as is consistent with baroclinically-generated circulation based on our analysis. For the 10 MPa wave, the phase of the interface inverts at, before the expansion hits, causing circulation deposited by the expansion to have the same sign as that deposited by the compression. For the 1 and 5 MPa waves interface phase inversion occurs after the expansion and consequently deposits circulation opposite that of the compression wave.

Figure 4.8 shows the interface amplitude and circulation histories for 5 and 10 MPa trapezoidal wave cases for $0 \leq t \leq 1000$. The perturbation amplitude history is plotted on logarithmically-scaled axes. For

both waves, the slope of the perturbation amplitude is approximately 0.60 long after the waves have left the interface. This is slightly higher than the 0.5 slope predicted by scaling law (4.16). The results for the 1 MPa trapezoidal wave were not included because interface evolved too slowly to obtain useful data given the computational resources available.

4.4.1.3 Circulation and vorticity dynamics

We observe that the wave deposits a sheet of vorticity along the interface that moves with the interface in time. Figure 4.5 shows a surface plot of vorticity in the region of the domain around the interface for the 10 MPa trapezoidal wave case, at $t = 1.0$, during the middle of the interface-compression wave interaction (Left). Not shown is the rest of the domain, where vorticity was relatively insignificant. The vorticity is antisymmetric across the $x = 0.5$ center line. To analyze the physical mechanisms generating the vorticity, we plot each term of the circulation generation equation (4.15) during the period around the compression wave-interface interaction. Near the end of the interaction at $t = 1.0$, $(\partial \Gamma / \partial t)_{advective} = -5.3 \times 10^{-5}$; $(\partial \Gamma / \partial t)_{compressible} = 2.7 \times 10^{-5}$; $(\partial \Gamma / \partial t)_{baroclinic} = 7.7 \times 10^{-3}$; $(\partial \Gamma / \partial t)_{total} = 7.7 \times 10^{-3}$. This result is quantitatively consistent with expected vorticity generation based on our analysis (4.13). Furthermore, it supports our hypothesis that vorticity is primarily baroclinically generated.

4.4.1.4 Dependence on the length of the wave

To investigate the dependence of the dynamics on the length of the trapezoidal wave L , and comparably the wave-interface interaction time, we compare results for $p_a = 10$ MPa waves of constant rise and fall length ΔL_a . This effectively changes the time the interface has to evolve while experiencing the constant elevated pressure portion of the wave between the compression and expansion. Figure 4.10 shows the interface amplitude and circulation histories corresponding to waves with $L = 45\lambda, 35\lambda, 30\lambda, 25\lambda, 15\lambda, 10\lambda$ for $0 \leq t \leq 25$. For the three longest waves, $L \geq 30\lambda$, the expansion encounters the interface after the perturbation reverses phase. In these cases, the expansion deposits additional positive circulation along the right half of the interface. For the shorter waves, $L \leq 25\lambda$, the expansion encounters the interface before the perturbation reverses phase and the net half-domain circulation is decreased. Comparing cases in which the interface inverts phase before the expansion occurs the larger $a(t)$ is at the time, the more circulation is generated. The same is true when comparing cases in which the phase inversion occurs after the interface inverts phase.

4.4.2 Interface response to Diagnostic Ultrasound (DUS) waves

To evaluate the relevance of our trapezoidal wave experiments we simulate a $p_a = 1, 5$ and 10 MPa DUS pulse waves (See Figure 4.4) impinging onto the water air interface. In figure 4.11 we illustrate the circulation and interface amplitude histories for the $p_a = 10$ MPa DUS like-pulse case. The post-wave interface dynamics are similar to those observed for trapezoidal wave cases. During the wave-interface interaction, the interface amplitude is compressed overall, but oscillations are observed in correspondence with the acoustic pulse oscillations. After the wave has left the interface, the perturbation amplitude continues to decrease until the interface undergoes a phase inversion, after which the perturbation amplitude grows for the remainder of the simulation. half-domain circulation oscillates during wave-interface interaction before settling to a nearly constant non-zero value after the wave has passed. We note that the total circulation deposited is of the same order of magnitude as that generated by the trapezoidal wave of the same amplitude and duration. Qualitatively similar results were observed for the 5 MPa case. For the one 1 MPa case, the evolution of the system was slow such that running the simulation long enough to obtain useful results was computationally prohibitive.

4.4.3 Further discussion of the results

For both the trapezoidal and DUS pulse acoustic waves, the pressure, velocity, and density return to initial, ambient conditions after the passing of the wave. As these waveforms are continuous, this implies that the integral of the pressure gradient ∇p at each point along the interface, over all time must be zero. Hence we surmise that if the interface remains unchanged during the interaction with the wave, as it would for a wave moving with infinite velocity, $\nabla \rho$ remains constant and the net baroclinic circulation deposited must be zero. Thus for any finite duration acoustic wave such as ours to deposit net baroclinic circulation upon an interface, the interface itself must deform during interaction with the wave. This deformation alters the misalignment of the pressure and density gradients at the interface causing positive and negative circulation deposited to not cancel out entirely. Note that this is unique to waves that begin and end at the same pressure. This is not the case for the traditional RMI problem, for which conditions do not return to their original state after the passage of the shock.

For the cases varying the length of the static elevated pressure in the trapezoidal wave we previously noted that whether the expansion increased or decreased the total half-domain circulation depended on whether it encountered the interface before or after the phase change. If indeed circulation is driving the deformation of the interface, then changes in the waveform that appear to have little effect on the interface dynamics during the wave-interface interaction period, may have far more significant impacts on the long term dynamics of the interface. To put this in the context of DUS, which uses repeated pulses, if ultrasonically-deposited circulation is causing deformation within the lungs, longer Pulse Durations (PDs) may allow for greater deformation and increased circulation deposition as a result of any individual pulse. If the system acts as we have modeled it, the Pulse Repetition Frequency (PRF) would determine the degree of interface deformation experienced by pulses subsequent to the first and may influence deformation and hemorrhage. Finally, in recognition of the limitations of this study, we note that the true physical nature of lung tissue is viscoelastic ([Bayliss & Robertson, 1939](#)), and neither viscosity nor elasticity is included in our model problems. While preliminary results with a Navier-Stokes code showed similar early time results, we expect that viscosity would dissipate circulation over a long enough period of time. Furthermore, elasticity may provide a mechanism by which the alveolar walls could resist deformation or retard to their original shape between pressure perturbations.

In the context of DUS, which uses repeated pulses, if ultrasonically-deposited circulation is causing deformation within the lungs, longer PDs may allow for greater deformation and increased circulation deposition as a result of any individual pulse. If the system acts as we have modeled it, the PRF would determine the degree of interface deformation experienced by pulses subsequent to the first and may influence deformation and hemorrhage. Finally, in recognition of the limitations of this study, we note that the true physical nature of lung tissue is viscoelastic ([Bayliss & Robertson, 1939](#)), and neither viscosity nor elasticity is included in our model problems. While preliminary results with a Navier-Stokes code showed similar early time results, we expect that viscosity would dissipate circulation over a long enough period of time. Furthermore, elasticity may provide a mechanism by which the alveolar walls could resist deformation or retard to their original shape between pressure perturbations.

4.5 Conclusions

This work is unique in that it demonstrates that acoustic waves may trigger significant deformation of perturbed liquid-gas interfaces over long periods of time. The driving mechanism behind this deformation is baroclinic vorticity, which occurs as a result of misalignment between the pressure gradient of the acoustic wave and density gradient of the perturbed interface. This mechanism arises as a result of nonlinear, compressible fluid mechanics, and cannot be predicted through traditional linear acoustics. We suggest

that nonlinear effects such as baroclinic vorticity are important at liquid-gas interfaces, such as those in the lungs, because of the sharp density discontinuities between air and tissue within the lungs. To demonstrate this we simulate acoustic waves with properties relevant to DUS impinging from water into air.

The work presented here supports the following three conclusions:(1) Baroclinic vorticity generated by acoustic waves within the DUS regime is capable of significantly deforming perturbed liquid-gas interfaces. We observed that much of the vorticity generated by the acoustic wave at the interface remains with the interface as it evolves and deforms even long after the passage of all acoustic waves. Part of this is attributed to a lack of physical mechanism for dissipating vorticity in the inviscid case considered. From dimensional analysis we find scaling law (4.16), suggesting that the interface perturbation amplitude will grow as $t^{0.5}$ for purely circulation driven growth. In our computed results we find the actual perturbation amplitude grows as $t^{0.6}$. This discrepancy does not appear to change between $t = 500$ and 1000 and may be a result of the inability of a global quantity Γ to completely describe $a(t)$ which is governed by local fluid mechanics. (2) During interactions between acoustic waves and perturbed liquid-gas interfaces, baroclinic vorticity is predominantly deposited in the gas-dominated fluid. We perform analysis to predict that on either side of an infinitely sharp water-air interface, the vorticity generation rate would be approximately two orders of magnitude greater on the air side of the interface than in the water. This is qualitatively supported by our computational results which find that near the end of the initial compression wave-interface interaction nearly all of the circulation exists in fluid dominated by air. For the 10 MPa wave, for instance, 97% of the circulation is found in fluid with volume fraction of water $\alpha < 0.5$ at $t = 1$, after 91% of the compression has passed. (3) Changes in the acoustic waveform that have little effect on the interface dynamics during their interaction can substantially effect the interface over longer periods of time, via vorticity. By comparing the effects of 10 MPa trapezoidal waves with varying static pressure durations between compression and expansion, we observe that the evolution of the interface between these two wave components drastically effects the ultimate growth rate of the interface. The phase and amplitude of the interface perturbation at the time it encounters the expansion wave determine the direction and magnitude respectively of the vorticity deposited. Consequently, the amount of vorticity remaining at the interface and in the surrounding fluid after the passage of the wave changes greatly based on the time-dependent features of the wave.

This work is a step toward understanding the effects of acoustically generated vorticity on gas-liquid interfaces, however we acknowledge that there are many questions left to be answered. However, we consider our findings in the context of DUS-induced LH and propose a previously unconsidered potential damage mechanism. We hypothesize that baroclinic torque occurs at fragile air-tissue interfaces of the lung due to misalignment between the US pressure gradient and material interface density gradient, causing stress, deformation, and ultimately rupture at the interface. We note that evaluation of the hypothesized damage mechanism will require considerable further work including experiments, and numerical simulations that incorporate realistic viscosity, elasticity, attenuation, and realistic waveforms and lung geometries. This validation is beyond the scope of the proposed dissertation.

4.6 Future Work

Finally, we address some of the limitations of this study and propose future work to address some of these issues. To further evaluate the relevance of the proposed damage mechanisms and presented results to DUS-induced lung hemorrhage, viscous and elastic effects should be considered, as both of these have the potential to reduce observed deformation, and mitigate hemorrhage. Additionally, geometries that more accurately represent physical networks of alveoli within the lungs will be useful to understand the propagation of ultrasound waves and hemorrhage deeper into the lungs, beyond the first tissue-air interface.

To do this accurately, it may be necessary to include a model for interface rupture. Many of these future tasks will require not only numerical efforts, but also experimental studies to appropriately characterize the lung tissue and validate the suggested models. Additionally, to increase our understanding of the relevant fluid dynamics, it would be useful to be able predict the circulation and interface dynamics based on the wave properties and initial conditions.

To address some of these issues and complete the proposed dissertation research we plan to perform several tasks:

- To further the relevance of this research to the problem of DUS of the lung we will:
 1. Calculate stresses and strains at the interface and compare to previously measured failure thresholds of the lungs. A passive viscous stress tensor will be computed from the velocity field and volume fraction fields, assuming constant viscosity for pure water and air. Either Volume fraction fields or Lagrange particles will be used to calculate the pathlength of the interface as a function of time $S_{Intf}(t)$ and engineering strain of the interface, ε_{Intf} , as though the interface were a solid sheet of tissue where, $\varepsilon_{Intf} = [S_{Intf}(t = 0) - S_{Intf}(t)]/S_{Intf}(t = 0)$.
 2. Investigate the effects of alveolar side wall structures. To model this, a thin layer of tissue (modeled as water) will be placed at the edges of the alveolus (modeled as air) and periodic boundary conditions will be used.
 3. Investigate the propagation of ultrasound waves and hemorrhage into the lungs. To model this we will modify the current geometry to such that a thin sinusoidal strip of water, parallel to the initial interface, will be placed every λ deep into the alveoli. This will be used with the alveolar walls described above to simulate a diagnostic ultrasound pulse propagating into a uniformly distributed alveolar network.
- To further our understanding of fluid mechanics associated with acoustically perturbed fluid interfaces we will:
 1. Seek to understand discrepancies between the $a(t) \sim \sqrt{\Gamma t}$ scaling obtained and the numerical results. This may require longer simulations to reach the final growth rate of the interface, or re-assessment of the logic behind using a global metric to describe a locally-dependent flow feature.
 2. Develop a model to predict the circulation deposited on a slightly perturbed interface by a simple compression or expansion wave. To do this, we will assume the interface is static during the interaction with the wave. Then, estimate the baroclinic term of the vorticity equation based on known interface and wave properties and linear acoustic relationships between state variables.
 3. Develop a model to predict the interface phase-reversal time for a simple compression wave. This model will be based on the expected compression of the interface due to the rising pressure during the interaction with the wave, and the subsequent circulation driven deformation described by scaling law (4.16).
 4. Design acoustic waveforms that utilize time dependent features and interface deformation to generate minimal circulation and interface growth. To do this, we will aim to create waves that deposit vorticity of opposite sign and approximately equal magnitude before and after the interface phase change. One example of a wave that will be considered is a single period sinusoidal pressure wave that changes from the compression to expansion as the phase of the interface inverts.

5. Investigate the cause of late time circulation growth observed in some simulations. As can be seen from the circulation history for the 10 MPa trapezoidal wave in Figure 4.8, circulation continues to grow after all waves have left the domain. We plan to first determine if this effect is physical or numerical. If this effect is physical, we aim to determine the mechanism.

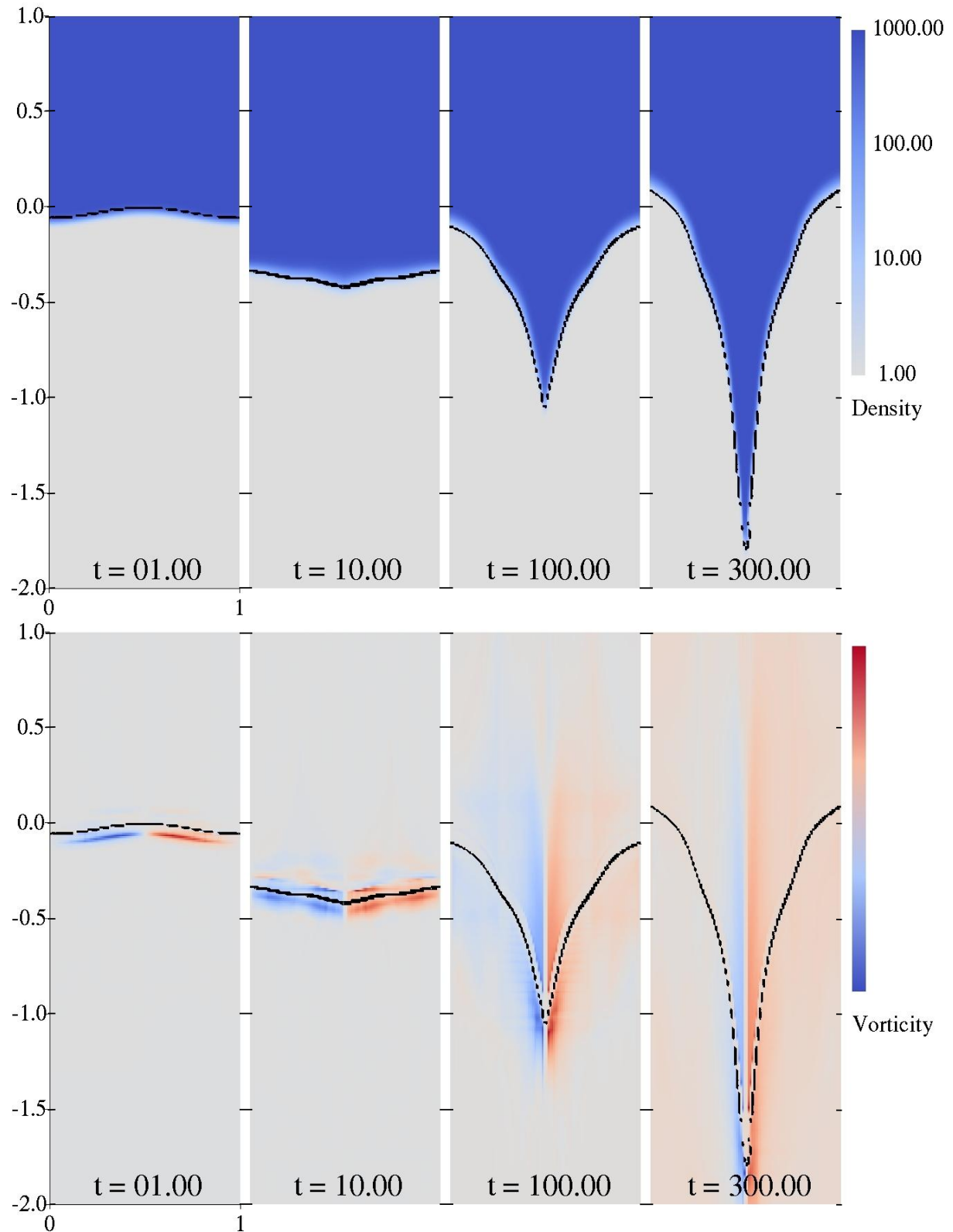


Figure 4.5: Surface plots of density (Top) and vorticity (Bottom) throughout the evolution of the interface for the 10 MPa trapezoidal wave case. Areas of high density (i.e., water) are indicated in dark blue. Areas of low density (i.e., air) are indicated in white. Positive (counterclockwise) vorticity is indicated in red, and negative (clockwise) vorticity can be seen in blue.

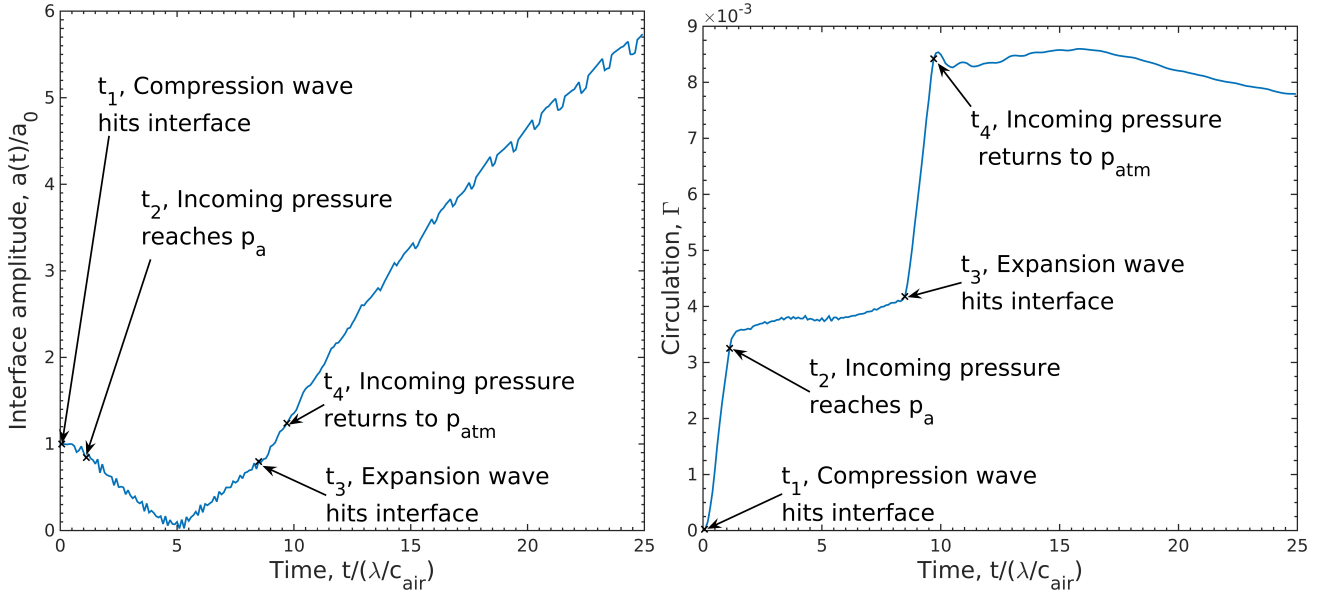


Figure 4.6: The interface amplitude (left) and circulation (right) histories corresponding to the 10 MPa trapezoidal waves are shown for $t \leq 25$. Indicated times, t_{1-4} , are the times at which different stages of the incoming trapezoidal pressure wave shown in Figure 4.4 first encounter the interface.

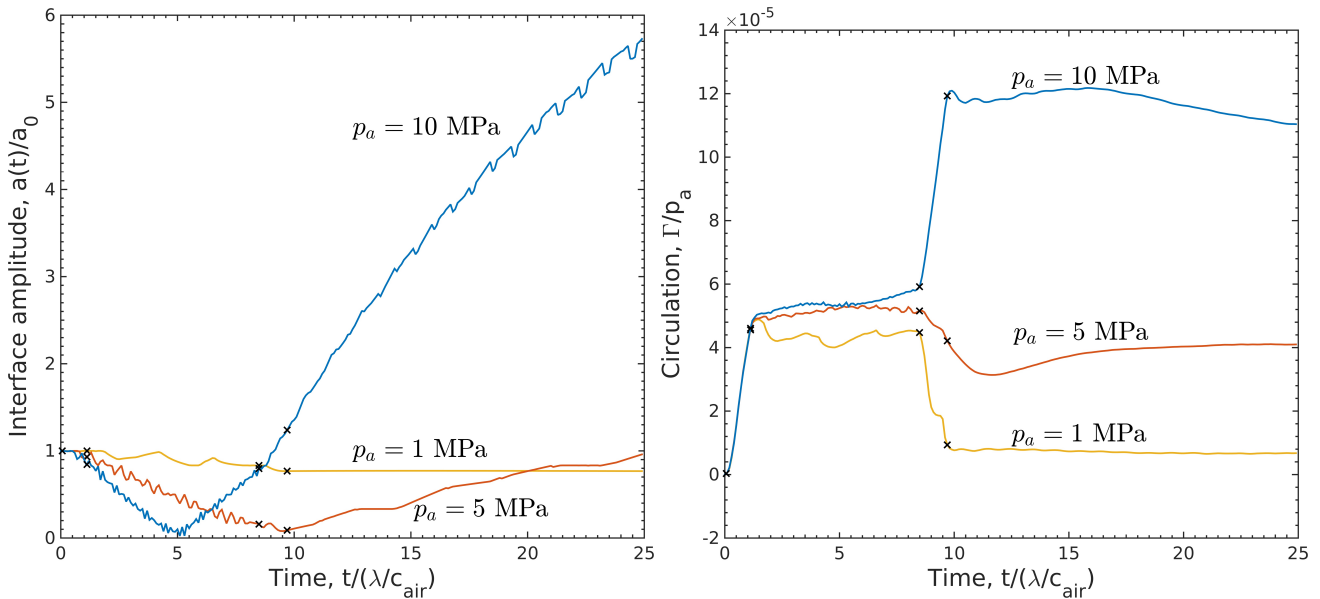


Figure 4.7: The interface amplitude (left) and circulation (right) histories corresponding to the 1(yellow), 5(orange), and 10(blue) MPa trapezoidal waves are shown for $t \leq 25$. The circulation history is normalized by the acoustic amplitude of the incoming wave to illustrate that circulation deposition by the compression wave scales linearly with p_a .

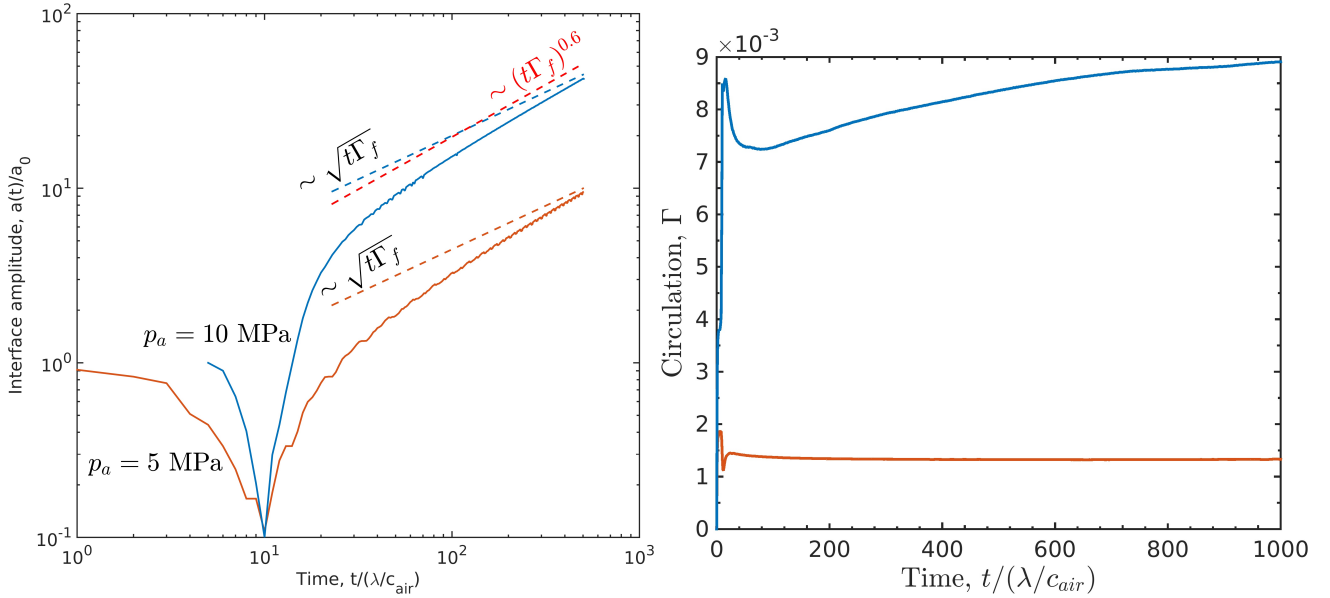


Figure 4.8: The interface amplitude (left) and circulation (right) histories corresponding to the 5(orange) and 10(blue) MPa trapezoidal waves are shown for $t \leq 500$. To appropriately compare late time dynamics, time has been offset in the interface amplitude history such that the phase reversal appears to occur simultaneously in both simulations. Dashed lines of the same color are used to demonstrate the expected slope of pure circulation driven interface growth, based on Equation (4.16). The red dashed line shows the slope we appear to be approaching for the 10 MPa wave case for the end time.

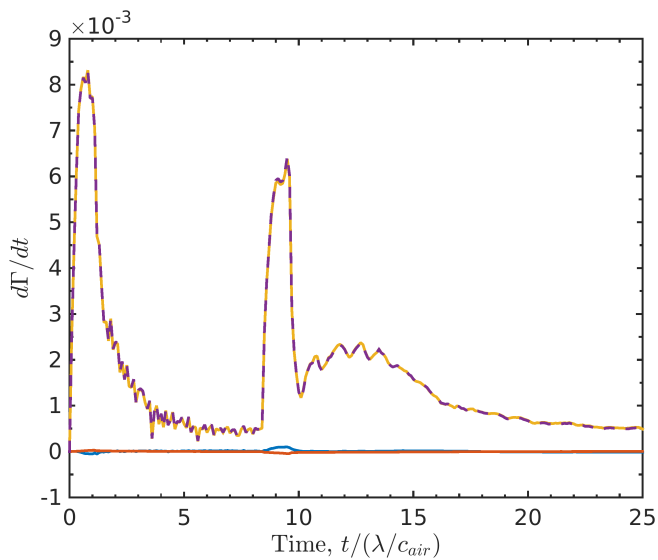


Figure 4.9: Each term of the circulation generation equation (4.15) is plotted as a function of time: $(d\Gamma/dt)_{advective}$ (blue), $(d\Gamma/dt)_{compressible}$ (orange), $(d\Gamma/dt)_{baroclinic}$ (yellow), $(d\Gamma/dt)_{total}$ (purple, dashed).

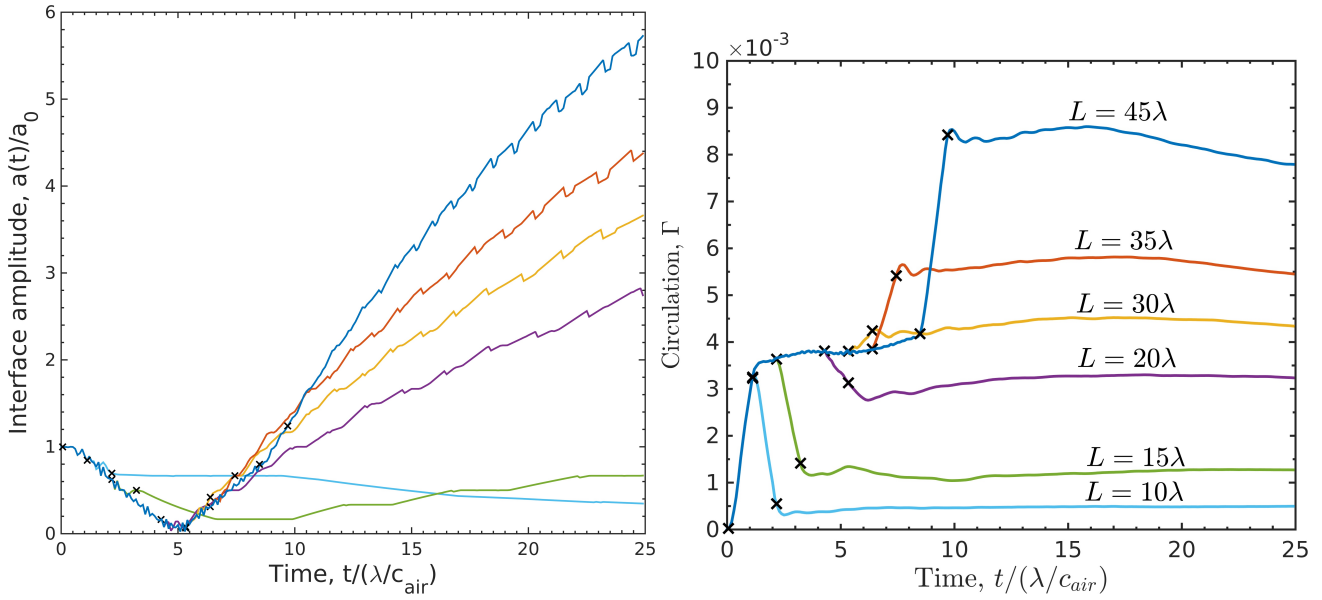


Figure 4.10: The interface amplitude (left) and circulation (right) histories for waves of varying total length L and elevated static pressure duration between the expansion and compression . Here we show results for $L = 45\lambda$ (blue), $L = 35\lambda$ (orange), $L = 30\lambda$ (yellow), $L = 20\lambda$ (purple), $L = 15\lambda$ (green), $L = 10\lambda$ (light blue)

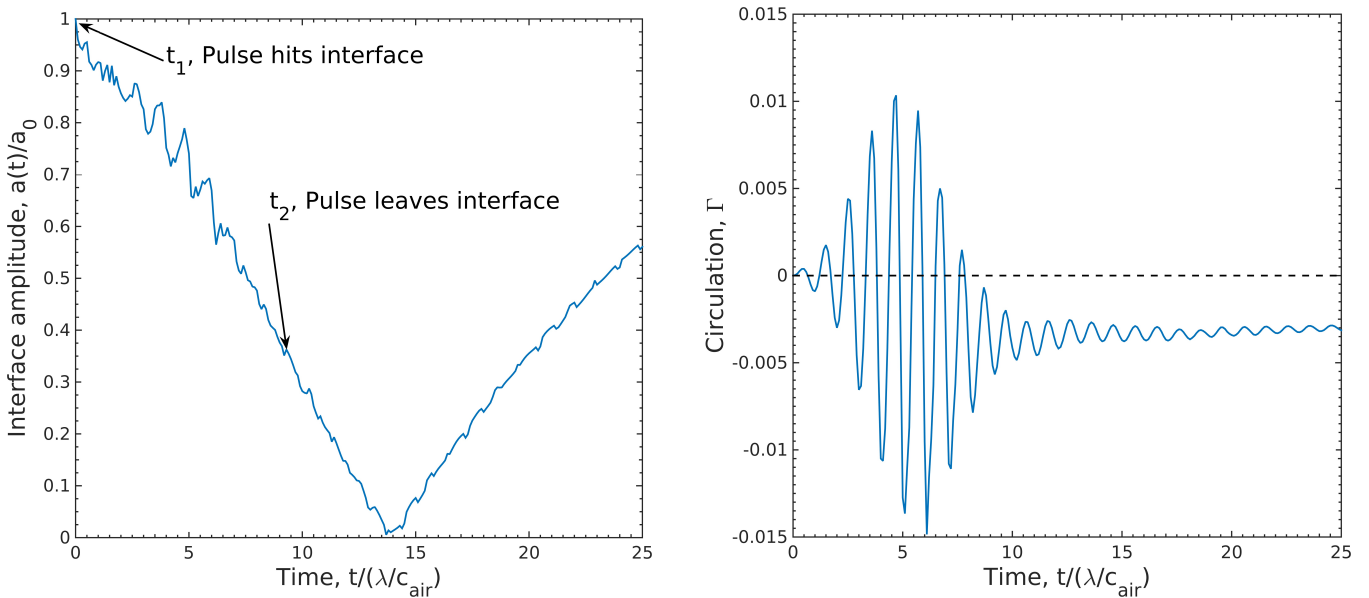


Figure 4.11: The interface amplitude (left) and circulation (right) histories corresponding to the a water-air interface disturbed by the US-like pulse shown in Figure 4.4.

Part II

**Estimating transmission loss uncertainty in
uncertain ocean environments.**

CHAPTER 5

Past work: Efficient estimation of the probability density function of transmission loss in uncertain ocean environments via area statistics

5.1 Abstract

Calculations of acoustic Transmission Loss (TL) in the ocean are useful in naval and ocean monitoring applications. These TL calculations are often uncertain because they are based on uncertain environmental parameters, but standard methods for determining TL uncertainty are computationally expensive. This paper describes how TL statistics in a range-depth area surrounding the point of interest within a single TL-field calculation can be efficiently used to estimate the Probability Distribution Function (PDF) of TL that results from ocean environment uncertainty. Such area-statistics estimated PDFs of TL are compared to PDFs of TL obtained from 1000-sample Monte-Carlo calculations at source frequencies of 100, 200 and 300 Hz and source depths of 91, 137, and 183 m in four different uncertain ocean environments at test location depths from 20 m to 5 km and source-receiver ranges from a few km to more than 60 km. These comparisons show that the estimated PDFs of TL are engineering-level accurate in 93% of tests in ocean environments with consistent bottom reflection, and can be produced with $O(10^{-6})$ the computational effort required for the Monte-Carlo calculations. In deep refracting environments, area statistics was engineering-level in 78% of test cases after algorithm adjustments.

A manuscript of this work is in preparation for submission.

BIBLIOGRAPHY

- Abgrall, Rémi. 1996. How to Prevent Pressure Oscillations in Multicomponent Flow Calculations: A Quasi Conservative Approach. *Journal of computational physics*, **125**(1), 150–160.
- Alahyari Beig, Shahaboddin, & Johnsen, Eric. 2015. Maintaining interface equilibrium conditions in compressible multiphase flows using interface capturing. *Journal of computational physics*, **302**(dec), 548–566.
- Anderson, John David. 1990. *Modern compressible flow: with historical perspective*.
- Apfel, R E. 1982. Acoustic cavitation: a possible consequence of biomedical uses of ultrasound. *The british journal of cancer supplement*, **5**(mar), 140–6.
- Baggs, R., Penney, D.P., Cox, C., Child, S.Z., Raeman, C.H., Dalecki, D., & Carstensen, E.L. 1996. Thresholds for ultrasonically induced lung hemorrhage in neonatal swine. *Ultrasound in medicine & biology*, **22**(1), 119–128.
- Bayliss, L. E., & Robertson, G. W. 1939. THE VISCO-ELASTIC PROPERTIES OF THE LUNGS. *Quarterly journal of experimental physiology and cognate medical sciences*, **29**(1), 27–47.
- Brouillette, Martin. 2002. The Richtmyer-Meshkov Instability. *Annual review of fluid mechanics*, **34**(1), 445–468.
- Brujan, Emil Alexandru. 2011. *Cavitation in non-newtonian fluids: With biomedical and bioengineering applications*. Berlin, Heidelberg: Springer Berlin Heidelberg.
- Child, S.Z., Hartman, C.L., Schery, L.A., & Carstensen, E.L. 1990. Lung damage from exposure to pulsed ultrasound. *Ultrasound in medicine & biology*, **16**(8), 817–825.
- Dalecki, Diane. 2004. Mechanical bioeffects of ultrasound. *Annual review of biomedical engineering*, **6**(jan), 229–248.
- Dalecki, Diane, Child, Sally Z., Raeman, Carol H., Cox, Christopher, & Carstensen, Edwin L. 1997. Ultrasonically induced lung hemorrhage in young swine. *Ultrasound in medicine and biology*, **23**(5), 777–781.
- Drake, Paul. 2006. *High-Energy-Density Physics*. Shock Wave and High Pressure Phenomena. Springer Berlin Heidelberg.
- Edelman, Sidney. 2005. *Understanding ultrasound physics*. Woodlands, Texas: ESP.
- Flynn, H. G. 1982. Generation of transient cavities in liquids by microsecond pulses of ultrasound. *The journal of the acoustical society of america*, **72**(6), 1926.

- Fraley, Gary. 1986. RayleighTaylor stability for a normal shock wave density discontinuity interaction. *Physics of fluids*, **29**(2), 376.
- Frizzell, Leon A., Chen, Ellen, & Lee, Chong. 1994. Effects of pulsed ultrasound on the mouse neonate: Hind limb paralysis and lung hemorrhage. *Ultrasound in medicine and biology*, **20**(1), 53–63.
- Frizzell, Leon A., Zachary, James F., O'Brien, William D., & O'Brien, William D. 2003. Effect of pulse polarity and energy on ultrasound-induced lung hemorrhage in adult rats. *The journal of the acoustical society of america*, **113**(5), 2912.
- Harrison, G.H. H, Eddy, H.A. A, Wang, J.-P. P, & Liberman, F.Z. Z. 1995. Microscopic lung alterations and reduction of respiration rate in insonated anesthetized swine. *Ultrasound in medicine & biology*, **21**(7), 981–983.
- Heifetz, E., & Mak, J. 2015. Stratified shear flow instabilities in the non-Boussinesq regime. *Physics of fluids*, **27**(8), 086601.
- Henry de Frahan, Marc T., Varadan, Sreenivas, & Johnsen, Eric. 2015. A new limiting procedure for discontinuous Galerkin methods applied to compressible multiphase flows with shocks and interfaces. *Journal of computational physics*, **280**(jan), 489–509.
- Holland, Christy K., Deng, Cheri X., Apfel, Robert E., Alderman, Jonathan L., Fernandez, Leonardo A., & Taylor, Kenneth J.W. 1996. Direct evidence of cavitation in vivo from diagnostic ultrasound. *Ultrasound in medicine & biology*, **22**(7), 917–925.
- Jacobs, J. W., & Sheeley, J. M. 1996. Experimental study of incompressible RichtmyerMeshkov instability. *Physics of fluids*, **8**(2), 405.
- Kinsler, Lawrence E., Frey, Austin R., Coppens, Alan B., & Sanders, James V. 1982. Fundamentals of Acoustics by Lawrence. *The journal of the acoustical society of america*, **72**(3), 1090.
- Kramer, J. M., Waldrop, T. G., Frizzell, L. A., Zachary, J. F., & O'Brien, W D. 2001. Cardiopulmonary function in rats with lung hemorrhage induced by pulsed ultrasound exposure. *Journal of ultrasound in medicine : official journal of the american institute of ultrasound in medicine*, **20**(11), 1197–1206.
- Latini, Marco, Schilling, Oleg, & Don, Wai Sun. 2007. Effects of WENO flux reconstruction order and spatial resolution on reshocked two-dimensional RichtmyerMeshkov instability. *Journal of computational physics*, **221**(2), 805–836.
- Lichtenstein, Daniel A. 2009. Ultrasound examination of the lungs in the intensive care unit. *Pediatric critical care medicine : a journal of the society of critical care medicine and the world federation of pediatric intensive and critical care societies*, **10**(6), 693–698.
- Meltzer, Richard S., Adsumelli, Rishi, Risher, William H., Hicks, George L., Stern, David H., Shah, Pratima M., Wojtczak, Jacek A., Lustik, Stewart J., Gayeski, Thomas E., Shapiro, Janine R., & Carstensen, Edwin L. 1998. Lack of Lung Hemorrhage in Humans After Intraoperative Transesophageal Echocardiography with Ultrasound Exposure Conditions Similar to Those Causing Lung Hemorrhage in Laboratory Animals. *Journal of the american society of echocardiography*, **11**(1), 57–60.
- Meshkov, E. E. 1972. Instability of the interface of two gases accelerated by a shock wave. *Fluid dynamics*, **4**(5), 101–104.

- Meyer, K. A. 1972. Numerical Investigation of the Stability of a Shock-Accelerated Interface between Two Fluids. *Physics of fluids*, **15**(5), 753.
- Miller, Douglas L., Dou, Chunyan, & Wiggins, Roger C. 2008. Frequency Dependence of Kidney Injury Induced by Contrast-Aided Diagnostic Ultrasound in Rats. *Ultrasound in medicine and biology*, **34**(10), 1678–1687.
- O'Brien, W.D., Jr., Simpson, D.G., Frizzell, L.A., & Zachary, J.F. 2001a. Age-dependent threshold and superthreshold behavior of ultrasound-induced lung hemorrhage in pigs. *2001 ieee ultrasonics symposium. proceedings. an international symposium (cat. no.01ch37263)*, **2**(6).
- O'Brien, W D, Frizzell, Leon A., Weigel, Ronald M., Zachary, James F., O'Brien, William D., Frizzell, Leon A., Weigel, Ronald M., & Zachary, James F. 2000. Ultrasound-induced lung hemorrhage is not caused by inertial cavitation. *The journal of the acoustical society of america*, **108**(3), 1290–1297.
- O'Brien, W.D., Simpson, D.G., Frizzell, L.A., & Zachary, J.F. 2001b. Superthreshold behavior and threshold estimates of ultrasound-induced lung hemorrhage in adult rats: role of beamwidth. *Ieee transactions on ultrasonics, ferroelectrics and frequency control*, **48**(6), 1695–1705.
- O'Brien, W.D., Simpson, D.G. Douglas G, Moon-Ho Ho, Miller, R.J. Rita J, Frizzell, Leon A L.A., Zachary, James F J.F., Brien, William D O, Simpson, D.G. Douglas G, Ho, Moon-ho, Miller, R.J. Rita J, Frizzell, Leon A L.A., Member, Senior, & Zachary, James F J.F. 2003a. Superthreshold behavior and threshold estimation of ultrasound-induced lung hemorrhage in pigs: Role of age dependency. *Ieee transactions on ultrasonics, ferroelectrics and frequency control*, **50**(2), 153–169.
- O'Brien, William D., & Miller, Douglas L. 2007. Ultrasound-biophysics mechanisms. *Progress in biophysics and molecular biology*, **93**(1-3), 212–255.
- O'Brien, William D, Frizzell, Leon A, Schaeffer, David J, & Zachary, James F. 2001c. Superthreshold behavior of ultrasound-induced lung hemorrhage in adult mice and rats: role of pulse repetition frequency and exposure duration. *Ultrasound in medicine & biology*, **27**(2), 267–277.
- O'Brien, William D., Kramer, Jeffrey M., Waldrop, Tony G., Frizzell, Leon A., Miller, Rita J., Blue, James P., & Zachary, James F. 2002. Ultrasound-induced lung hemorrhage: Role of acoustic boundary conditions at the pleural surface. *The journal of the acoustical society of america*, **111**(2), 1102.
- O'Brien, William D., Simpson, Douglas G., Frizzell, Leon a., & Zachary, James F. 2003b. Threshold estimates and superthreshold behavior of ultrasound-induced lung hemorrhage in adult rats: Role of pulse duration. *Ultrasound in medicine and biology*, **29**(11), 1625–1634.
- O'Brien, William D., Simpson, Douglas G., Frizzell, Leon A., & Zachary, James F. 2005. Superthreshold behavior of ultrasound-induced lung hemorrhage in adult rats: Role of pulse repetition frequency and exposure duration revisited. *Journal of ultrasound in medicine*, **24**(3), 339–348.
- O'Brien, William D. W.D., & Zachary, J.F. 1997. Lung damage assessment from exposure to pulsed-wave ultrasound in the rabbit, mouse, and pig. *Ieee transactions on ultrasonics, ferroelectrics and frequency control*, **44**(2), 473–485.
- O'Brien, William D., Jr, Simpson, Douglas G., Frizzell, Leon A., & Zachary, James F. 2006. Superthreshold Behavior of Ultrasound-Induced Lung Hemorrhage in Adult Rats: Role of Pulse Repetition Frequency and Pulse Duration. *J. ultrasound med.*, **25**(7), 873–882.

- Patterson, Brandon, Miller, Douglas, & Johnsen, Eric. 2012. Theoretical microbubble dynamics in a homogeneous viscoelastic medium at capillary breaching thresholds. *The journal of the acoustical society of america*, **131**(4), 3385–3385.
- Penney, D.P., Schenk, E.A., Maltby, K., Hartman-Raeman, C., Child, S.Z., & Carstensen, E.L. 1993. Morphological effects of pulsed ultrasound in the lung. *Ultrasound in medicine & biology*, **19**(2), 127–135.
- Raeman, Carol H., Child, Sally Z., & Carstensen, Edwin L. 1993. Timing of exposures in ultrasonic hemorrhage of murine lung. *Ultrasound in medicine & biology*, **19**(6), 507–512.
- Raeman, C.H., Child, S.Z., Dalecki, D., Cox, C., & Carstensen, E.L. 1996. Exposure-time dependence of the threshold for ultrasonically induced murine lung hemorrhage. *Ultrasound in medicine & biology*, **22**(1), 139–141.
- Richtmyer, R.D. 1960. Taylor Instability in Shock Acceleration of Compressible Fluids. *Communications on pure and applied mathematics*, **XIII**, 297–319.
- Sadot, O., Erez, L., Alon, U., Oron, D., Levin, L. A., Erez, G., Ben-Dor, G., & Shvarts, D. 1998. Study of Nonlinear Evolution of Single-Mode and Two-Bubble Interaction under Richtmyer-Meshkov Instability. *Physical review letters*, **80**(8), 1654–1657.
- Samtaney, Ravi, & Zabusky, Norman J. 1994. Circulation deposition on shock-accelerated planar and curved density-stratified interfaces: models and scaling laws. *Journal of fluid mechanics*, **269**(-1), 45.
- Shyue, Keh-Ming. 2001. A Fluid-Mixture Type Algorithm for Compressible Multicomponent Flow with MieGrüneisen Equation of State. *Journal of computational physics*, **171**(2), 678–707.
- Tarantal, Alice F., & Canfield, Don R. 1994. Ultrasound-induced lung hemorrhage in the monkey. *Ultrasound in medicine & biology*, **20**(1), 65–72.
- Taylor, G. 1950. The Instability of Liquid Surfaces when Accelerated in a Direction Perpendicular to their Planes. I. *Proceedings of the royal society a: Mathematical, physical and engineering sciences*, **201**(1065), 192–196.
- Tjan, K. K., & Phillips, W. R. C. 2007 (mar). *On impulsively generated inviscid axisymmetric surface jets, waves and drops*.
- Tjan, K.K., & Phillips, W.R.C. 2008. On the impulsive generation of drops at the interface of two inviscid fluids. *Proceedings of the royal society a: Mathematical, physical and engineering sciences*, **464**(2093), 1125–1140.
- Zachary, J. F., & O'Brien, W. D. 1995. Lung Lesions Induced by Continuous- and Pulsed-Wave (Diagnostic) Ultrasound in Mice, Rabbits, and Pigs. *Veterinary pathology*, **32**(1), 43–54.
- Zachary, James F., Frizzell, Leon a., Norrell, Kandice S., Blue, James P., Miller, Rita J., O'Brien, William D., & O'Brien, William D. 2001a. Temporal and spatial evaluation of lesion reparative responses following superthreshold exposure of rat lung to pulsed ultrasound. *Ultrasound in medicine and biology*, **27**(6), 829–839.

Zachary, James F., Blue, James P., Miller, Rita J., Ricconi, Brian J., Eden, J. Gary, & O'Brien, William D. 2006. Lesions of ultrasound-induced lung hemorrhage are not consistent with thermal injury. *Ultrasound in medicine and biology*, **32**(11), 1763–1770.

Zachary, J.F., Sempsrott, J.M., Frizzell, L.A., Simpson, D.G., & O'Brien, W.D. 2001b. Superthreshold behavior and threshold estimation of ultrasound-induced lung hemorrhage in adult mice and rats. *Ieee transactions on ultrasonics, ferroelectrics and frequency control*, **48**(2), 581–592.

Zhang, Qiang, & Sohn, Sung-Ik. 1997. Nonlinear theory of unstable fluid mixing driven by shock wave. *Physics of fluids*, **9**(4), 1106.